University of Nevada, Reno

High-Purity Solid Parahydrogen

A thesis submitted in partial fulfillment of the
requirements for the degree of Master of Science in Physics

by

Ashok Bhandari

Dr. Jonathan D. Weinstein/Thesis Advisor

August, 2021

THE GRADUATE SCHOOL

We recommend that the thesis
prepared under our supervision by

ASHOK BHANDARI

entitled

High-purity solid parahydrogen

be accepted in partial fulfillment of the
requirements for the degree of

MASTER OF SCIENCE

Jonathan D. Weinstein, Ph.D.
Advisor

Thomas G. White, Ph.D.
Committee Member

Robert Sheridan, Ph.D.
Graduate School Representative

David W. Zeh, Ph.D., Dean
Graduate School

August, 2021

Abstract

Alkali atoms trapped in solid hydrogen matricies have demonstrated ultralong electron spin coherence times, and are promising as quantum sensors. Their spin coherence is limited by magnetic noise from naturally-occurring orthohydrogen molecules in the parahydrogen matrix. In the gas phase, the orthohydrogen component of hydrogen can be converted to parahydrogen by flowing it over a catalyst held at cryogenic temperatures, with lower temperatures giving a lower orthohydrogen fraction. In this work, we use a single cryostat to reduce the orthohydrogen fraction of hydrogen gas and grow a solid matrix from the resulting high-purity parahydrogen. We demonstrate operation of the catalyst down to a temperature of 8 K, and we spectroscopically verify that orthohydrogen impurities in the resulting solid are at a level $< 10^{-6}$. We also find that, at sufficiently low temperatures, the cryogenic catalyst provides isotopic purification, reducing the HD fraction.

To my parents

Acknowledgments

It is my pleasure to acknowledge all the persons who have provided their continuous guidance and valuable suggestions during my study and research at the University of Nevada, Reno.

First of all, I would like to thank my advisor, Dr. Jonathan Weinstein, for giving me this great research opportunity. I have gained knowledge and wonderful experiences during my research period. I am pretty much sure the experiences during the project would not be this exciting and interesting without him. I am grateful for his extraordinary guidance and patience.

I am thankful to our previous lab member Sunil Upadhyay for his support and help in the laboratory. I also want to thank Kyle Hardman for his experimental apparatus and Levi Ratto for his contribution to redesigning it for being able to perform this experiment. I am thankful to Alex Rollings for sharing this experimental effort. I am also thankful to my other lab members Ugne Dargyte and David Lancaster for their valuable help and suggestions during the lab.

My sincere thanks go to my thesis committee members for serving on my committee. I also want to thank all my professors for their excellent coursework that allowed me to understand the underlying concepts easily.

Most importantly, I would like to thank my family and friends for their unconditional love, support and motivation throughout this period.

Contents

Citation to Previously Published Work

Portions of this thesis have appeared previously in the following paper:

Bhandari, A., Rollings, A. P., Ratto, L., & Weinstein, J. D. (2021). High-purity solid parahydrogen. *Review of Scientific Instruments*, 92(7), 073202.

Chapter 1

Introduction

The study of atoms and molecules is crucial for the advancement of quantum technology. The study of atoms in the gas phase is extremely difficult due to their motion and collisions. Trapping of atoms eliminates the atomic motion and hence facilitates their study. "Matrix isolation" is a technique that involves the trapping of atoms and molecules within a solid host– a weakly-bound inert 'matrix'. Compared to other various trapping techniques like laser trapping, magnetic trapping, etc., the matrix isolation technique can trap atoms at high density and thus has a higher statistical sensitivity [1]. However, a solid host matrix can perturb the implanted atoms and destroy the properties of our interest. Thus, the host matrix for matrix isolation experiments should be so chosen that it ideally preserves the favorable properties of the implanted atoms or molecules.

Argon (Ar) and neon (Ne) solids have been used as matrices for matrix isolation experiments in the past to study the optical pumping and radiative properties of rubidium (Rb) atoms trapped inside them [2, 3]. Solid parahydrogen also has been shown to be an excellent host matrix. Because their interaction with the host matrix is weak, implanted

atoms and molecules retain much of their gas-phase properties. Parahydrogen matrix isolation experiments have traditionally been used to perform molecular spectroscopy; very narrow lines have been observed in infrared spectroscopy [4]. Recent experiments have shown that atoms trapped in solid hydrogen also retain their key properties for use as quantum sensors for magnetic fields: it is possible to control and measure the spin states of the implanted atoms through optical techniques [1, 5], and the trapped atoms exhibit both long ensemble spin dephasing times (T_2^*) [5, 6] and long spin coherence times (T_2) [7]. The atoms with long spin coherence times (T_2) and long ensemble spin dephasing times (T_2^*) have important applications in magnetometry, quantum sensing, and fundamental physics experiments [8, 9, 10, 11]. This thesis describes an experiment to grow a highly pure solid parahydrogen which has a promising scope as a matrix in the matrix isolation experiments.

In the first section of this chapter, we discuss the fundamental properties of the hydrogen molecule and its possible nuclear states. The second section contains the motivation for the work presented in this thesis. The prior experiments of concern are discussed in the third section. The last section provides a summary of the contents of the subsequent chapters.

1.1 Hydrogen molecule

Solid hydrogen is a quantum solid that possesses distinguishable properties from other molecular solids. Unlike other (molecular) solids, the rotational motions of the atoms or molecules isolated in solid hydrogen experience minimal perturbations due to interactions with the matrix [12]. If atoms or molecules are trapped within solid hydrogen, they experience translational localization at their respective lattice sites. However, their rotational motion is undistorted by the solid hydrogen matrix as low as T = 0 K. This

is mainly due to the large intermolecular distances between molecules in the solid. At zero-pressure solid density of 2.6×10^{22} cm^{-3}, the intermolecular distance of its nearest neighbor is 3.79 Å [12].

The ground state of the H_2 molecule exhibits no net electronic angular momentum, and hence the net magnetic moment due to electrons is absent. But, the molecule can exist in two possible nuclear spin states: orthohydrogen (I=1) and parahydrogen (I=0). They are characterized by odd and even rotational quantum numbers respectively. These odd and even rotational numbers for orthohydrogen and parahydrogen are governed by the requirement that the total wave function should be antisymmetric under particle exchange. Figure 1.1 presents the molecular rotational energy levels for an isolated H_2 molecule.

The even rotational numbers for parahydrogen imply a spherically symmetric (isotropic s- orbital) charge distribution for its ground state. Whereas the odd rotational numbers for orthohydrogen imply an anisotropic charge distribution (p-orbital) for the ground state as represented in figure 1.1.

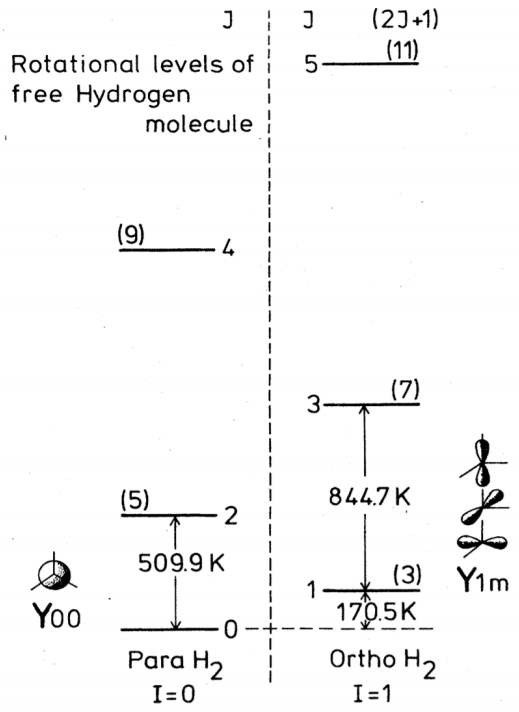

FIG. 4. The molecular rotational energy levels for an isolated H_2 molecule. The same diagram applies to D_2 but scaled down by about a factor of 2 due to the larger moment of inertia. The angular distribution of the two lowest rotational states are also indicated (Y_{10} and $Y_{11} \pm Y_{1-1}$ are actually shown). I is the total nuclear spin. Numbers in parenthesis are the m degeneracies.

Figure 1.1: The schematic of rotational energy levels of orthohydrogen and parahydrogen molecule. J and I are rotational and nuclear spin quantum numbers respectively, and the number in parenthesis are the degeneracies of the J levels. The figure is reproduced from reference [12].

1.2 Motivation

Alkali atoms trapped in solid parahydrogen exhibit long spin coherence times (T_2) [7] and long ensemble dephasing times (T_2^*) [5, 6]. However, the coherence time T_2 of the electron spin states of the implanted atoms was found to be limited by orthohydrogen impurities in the solid [7]. This is shown in figure 1.2. The electron spin coherence times (T_2) for rubidium increases by an order of magnitude when the orthohydrogen fraction changes from 10^{-2} to 10^{-4}. A similar dependence of electron spin coherence

time on orthohydrogen fraction was observed for cesium atoms.

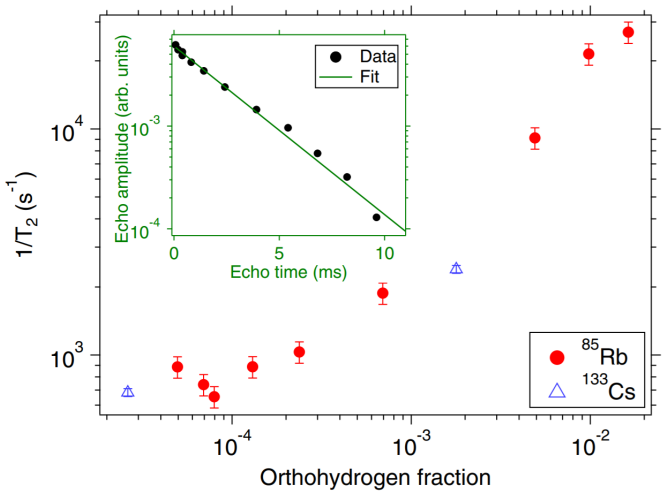

FIG. 2. The inset shows Hahn echo data for ^{85}Rb, for a superposition of the $m_F = -1$ and $m_F = 0$ levels, fit to exponential decay. The main graph shows the measured decoherence rates ($1/T_2$) for different crystals, taken by traditional Hahn echo sequences with unresolved m_F transitions, as described in the text. Rb data taken at a magnetic field of 13 G; Cs data taken at 22 G. The orthohydrogen fraction is typically known to within $\pm 25\%$.

Figure 1.2: Electron spin coherence times of rubidium and cesium atoms trapped in solid parahydrogen, plotted as a function of the orthohydrogen concenteration in the matrix. The figure is reproduced from reference [7].

In nuclear magnetic resonance (NMR) experiments performed previously with solid parahydrogen, the nuclear spin dephasing time T_2^* for HD molecules trapped in the matrix were also found to be limited by orthohydrogen impurities [13, 14]. Figure 1.3 shows the dependence of the linewidth of HD molecule with the orthohydrogen fraction in the matrix.

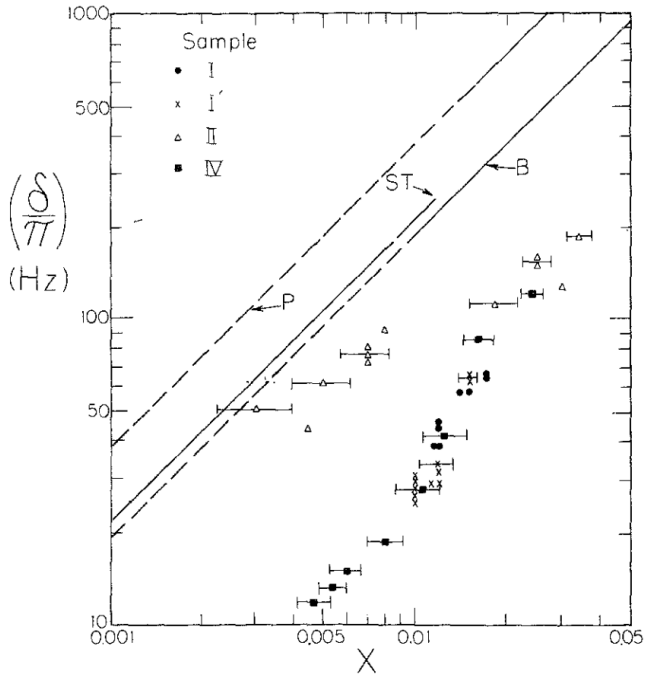

Fig. 9. Ortho-H_2 concentration dependence of the HD linewidth (full width at half maximum, δ/π) for four crystals at $T < 0.05$ K, where X decreased with time by ortho–para conversion. (For crystal II, this decrease took place over a period of 5 months.) The data refer to an "equilibrium" state where clustering has been completed. The solid and dashed lines labeled ST, P, and B refer, respectively, to the statistical result, the data by Pedroni *et al.*,[15] and the data by Buzerak *et al.*,[16] Eqs. (7a)–(7c).

Figure 1.3: The linewidth (FWHM) for HD molecules trapped in solid parahydrogen, plotted as a function of the orthohydrogen concenteration in the matrix. The figure is reproduced from reference [13].

Conversion of orthohydrogen to parahydrogen

To check whether the electron and nuclear spin coherence times get significantly better at low orthohydrogen impurities, it is crucial to prepare highly pure parahydrogen samples with an extremely low orthohydrogen fraction.

From the splittings of the energy levels of molecular hydrogen [15], we can theoretically calculate the equilibrium fraction of ortho molecules f_{ortho} at a temperature T. In the low-temperature limit, we can restrict our considerations to the lowest two energy levels. In that case, the expression for equilibrium ortho fraction f_{ortho} in terms of temperature

T is:

$$f_{\text{ortho}} = \frac{9\ \mathrm{e}^{-(170.5K)/T}}{1 + 9\ \mathrm{e}^{-(170.5K)/T}} \tag{1.1}$$

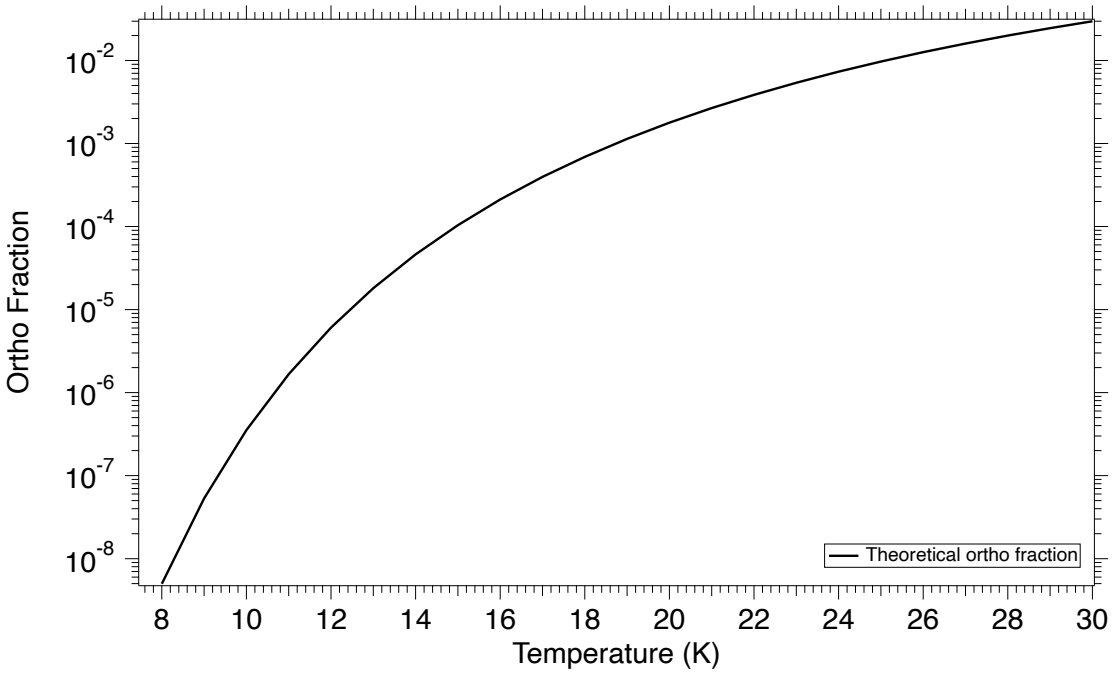

Figure 1.4: The theoretical ortho fraction in thermal equilibrium vs the temperature, as given by equation 1.1.

Figure 1.4 represents the dependence of equilibrium ortho fraction on the temperature. In the low temperature limit, the equilibrium ortho fraction drops exponentially with temperature.

In the absence of catalyst, the conversion of a hydrogen molecule between the orthohydrogen and parahydrogen states is extremely slow, even in the solid phase [12, 16, 17]; for the range of ortho concentrations presented in this thesis, there is negligible ortho to para conversion (OP conversion) on the timescale of days.

However, this conversion can be speed up by passing hydrogen gas over the paramagnetic catalyst (e.g. iron oxide or alumina). The paramagnetic catalyst provides a

magnetic field gradient for the orthohydrogen molecule to change its nuclear spin from I=1 to I=0 [18, 19]. If we expose the hydrogen gas to the catalyst for a sufficiently long time, the orthohydrogen and parahydrogen fractions should attain thermal equilibrium [15, 20]. The ortho fraction of the hydrogen gas after passing through the catalyst depends on the catalyst's temperature [21, 22].

1.3 Survey of prior work

In this section, we discuss the prior experiments performed to grow highly pure parahydrogen samples and their achieved results.

In 1993, Oka prepared a high purity parahydrogen crystal in an enclosed cell maintained at $\sim$ 7 K. The OP converter tube was filled with APACHI nickel silica gel and was immersed in liquid H_2 or helium in a separate dewar. He could grow samples up to 11.5 cm thick in this setup. Varying the OP converter temperature, he prepared different samples with ortho fractions ranging between 2×10^{-3} and 5×10^{-4} [23].

Tam and Fajardo in 1999 performed rapid vapor deposition experiments to grow high purity parahydrogen samples. They grew millimeters thick optically transparent samples with a flow rate of 120 sccm, with the OP converter maintained at 15 K. The conversion of ortho to para is done by passing the pre-cooled hydrogen gas through the APACHI catalyst in the OP converter. They used two separate cryostats in their experiment– one to cool the OP converter and the other to cool the substrate. The gas– after passing through the catalyst– was deposited on the substrate held at 2.5 K. Using infrared absorption spectra, they spectroscopically verified that the ortho fraction for their samples were less than 1×10^{-4} [24].

In 2004, Lee et al. performed pulsed deposition of parahydrogen molecules onto the substrate to grow solid parahydrogen samples. This method could allow growing solid

parahydrogen samples at the substrate temperature as high as 5.5 K. He used $Fe(OH)_3$ catalyst maintained at 25 K for the OP conversion [25].

Andrews and Wang in 2004 attempted simultaneous condensation and OP conversion to grow parahydrogen samples. Converted samples are sublimed directly from the 12–16 K catalyst to the 4 K matrix substrate. The best they reported was sublimating a 13 K solid sample which resulted in the formation of a sample with an ortho fraction of 1.9×10^{-3} [26]. Note that this is more than the expected ortho fraction corresponding to the OP converter temperature of 13 K.

In 2009, Tom et al. performed rapid vapor deposition experiments that were conceptually similar to the experiment performed by Tam and Fajardo [24]. It was a standalone system that could grow the samples at flow rates of 400 sccm. They were able to grow a parahydrogen sample with OP converter temperature maintained at 13.9 K, yielding the ortho fraction less than 1×10^{-4} [27].

Sundararajan et al. in 2016 used the OP converter similar to the converter designed by Momose (2009) to grow parahydrogen samples with OP converter temperature maintained at 13.5 K and measured the ortho fraction of their sample as 7×10^{-3} [28].

In 2020, Tsuge and Lee operated the OP converter at 13 K with a flow rate of 30 sccm to prepare parahydrogen gas. For the OP conversion, they built a similar system to the system built by Tam and Fajardo [24]. After the OP conversion, the parahydrogen gas is mixed with the guest molecules and deposited onto a substrate. There is a possibility of back conversion of parahydrogen to orthohydrogen during the the preparation of a gaseous mixture and matrix deposition. So they expect the ortho fractions for the sample they deposited to be higher than the ortho fraction expected from the temperature of the catalyst [29].

The experiments to grow parahydrogen samples were performed in our lab in the past.

The previous experimental set-up to grow parahydrogen samples in our lab is presented in Andrew Kanagin's thesis [30]. With that experimental setup, the parahydrogen samples with an orthohydrogen fraction of 9×10^{-3} could be grown with an OP converter held at a temperature around 20 K. In this work, with a slightly modified apparatus, we have employed a similar technique to operate our OP converter at significantly lower temperatures to grow significantly high purity parahydrogen samples.

1.4 Organization of the thesis

In this section, we briefly describe the contents that appear in the following chapters.

In chapter 2, we describe various parts of the apparatus that were used for our experiment. All the non-cryogenic and cryogenic parts of our apparatus are sorted and explained in detail. We also discuss the catalyst used for converting orthohydrogen to parahydrogen. At the end of this section, we briefly discuss the data acquisition and analysis method used for the experiment.

Chapter 3 is the description of the experimental setup and sample growth. Starting from the description of the experimental setup and sample growth conditions, we present the data for the partial pressures inside the chamber. At the end of this chapter, we discuss the observed delay in the deposition of the hydrogen gas onto the substrate quantitatively.

In chapter 4, we present the spectrum of solid hydrogen and discuss how we can extract information about the sample thickness, ortho fraction, and HD fraction from the spectrum.

Chapter 5 presents the results of our experiment. We present the data of achieved sample growth rates, ortho fractions, and HD fractions for all the samples grown during

our experiment. It also includes the discussion about how well the data agrees with the expected numbers and discuss our results in case of low signal-to-noise data.

In chapter 6, we discuss the attempts made to grow the sample at higher flow rates.

Chapter 7 provides the conclusions for our work in terms of growing higher purity parahydrogen samples and related future works.

Chapter 2

Apparatus

The schematic of the apparatus is shown in figure 2.1. The coldfinger, the second-stage OP converter, and their thermal links to the second stage of the pulse-tube cooler are surrounded by a radiation shield thermally connected to the first stage of the pulse-tube cooler. Three layers of aluminized mylar are placed on the outer surface of the radiation shields, which prevents black-body radiation from entering from the room temperature vacuum chamber to the cold parts inside the chamber. All this is contained within a vacuum chamber formed from ISO 400 nipples. The vacuum chamber, radiation shield, and the copper heatlinks between the pulse-tube cooler and the cold finger were all inherited from a prior experiment described in Kyle Hardman's thesis [31]. We have made a few modifications in the prior apparatus to allow for the growth of high-purity parahydrogen solids: we have added the cold finger plate, cold finger, substrate, and H_2 plumbing. We provide the detailed description of all the relevant parts in the following sections.

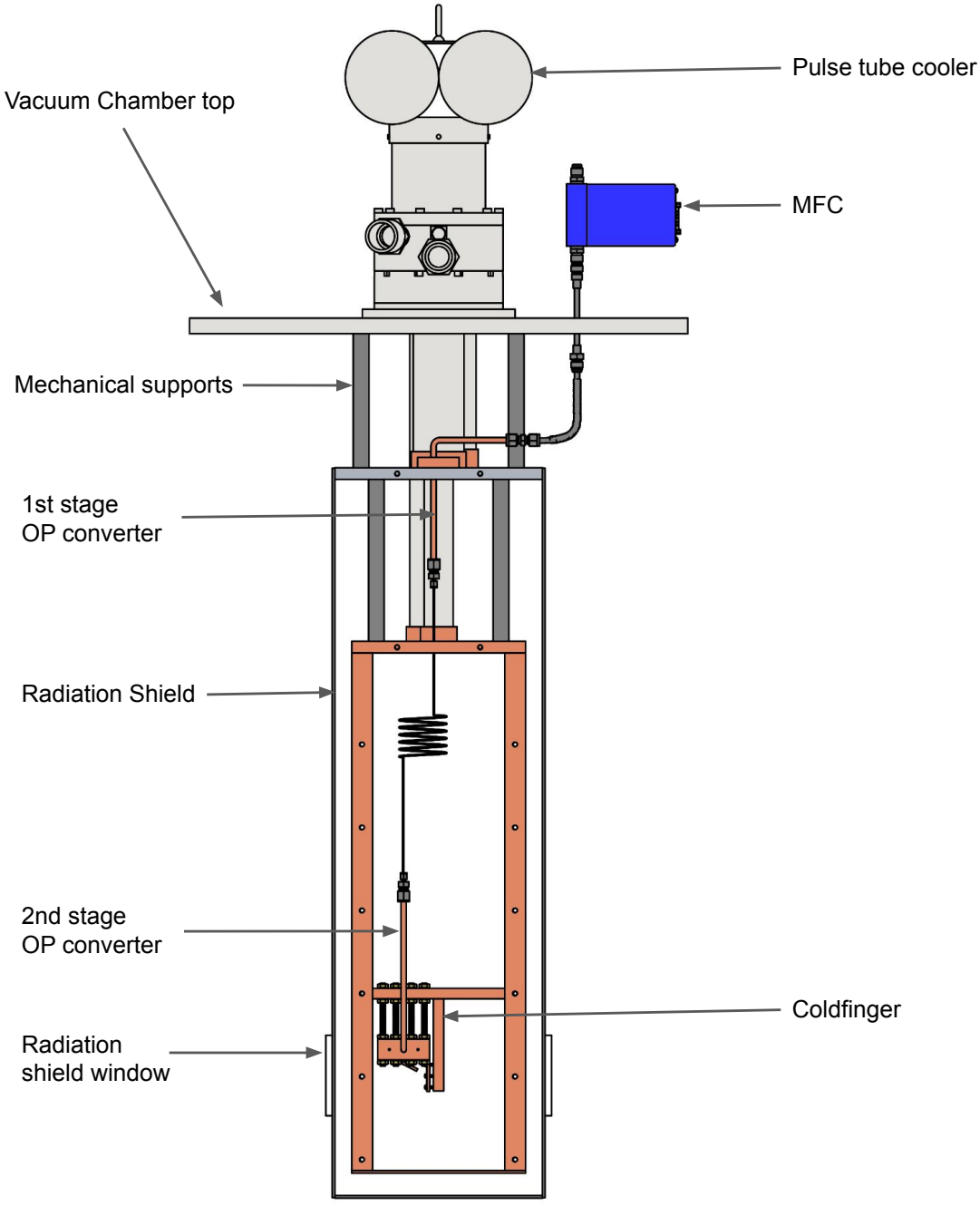

Figure 2.1: Schematic of the apparatus. The vacuum chamber is omitted for clarity, and various elements and vacuum feedthroughs have similarly been simplified or omitted.

2.1 Non-cryogenic parts

2.1.1 Vacuum Pumps

We used a roughing pump and a turbomolecular pump to evacuate the chamber. The roughing pump is used to pump out the chamber at high pressures. When the pressure inside the chamber reaches < 0.5 Torr, the roughing pump is backing the turbomolecular pump. The turbomolecular pump used for our experiment is TwisTorr 84 FS which has a nominal pumping speed of 80 L/s [32]. During deposition, we keep both pumps running. Although most of our pumping is cryo pumping from the cold surfaces in our chamber, the turbopump evacuates the small amount of helium gas present in the hydrogen gas.

2.1.2 Thermometry

There are five temperature sensors to measure the temperature of different parts inside the cryostat. Four of them are DT-670 silicon diode (Band B1) sensors from Lakeshore Cryotronics, located on the cryocooler second stage, cold finger plate, cold finger, and first stage cold plate. They have a tolerance of $\pm$ 0.5 K for the temperature range of our interest. The fifth sensor is a S950 silicon diode sensor (uncalibrated) from Cryo-Con. It has a tolerance of $\pm$ 0.2 K for the temperature range of our interest. We placed the S950 silicon diode sensor on the copper block of the second-stage OP converter. A constant current circuit in the electronics box (described in section 2.1.6) supplies 10 μA current to all these sensors. The temperature is determined from the resulting voltage drop [33, 34]. We monitored and logged these voltage drops using a LabVIEW program (described in section 2.4).

2.1.3 Pressure measurements

We monitored the chamber pressure using a 910 DualTrans Transducer from MKS instruments [35]. It is mounted on the top of the vacuum chamber. The data from this pressure sensor is acquired and recorded using the data acquisition technique as explained in section 2.4. This pressure sensor is used for pressure measurements from atmospheric pressure to 10^{-4} Torr.

Figure 2.2: The commercial pressure sensor used for our experiment.

To measure the chamber pressure below 10^{-4} Torr, we used a Residual Gas Analyzer (RGA) [36]. It also measures the partial pressure of different gas molecules inside the chamber. The RGA measurements were performed before each sample growth to have

an estimate of the background vacuum. The ion-gauge readouts of the background vacuum were on the order of 10^{-8} Torr. The partial equilibrium pressure of H_2 was typically on the order of 10^{-9} Torr, and that of He is $< 10^{-10}$ Torr. During the sample growths (when hydrogen is flowing into the chamber), we continued pumping on the chamber, and the equilibrium chamber pressures were on the order of 10^{-7} Torr. The partial equilibrium pressures of H_2 and He are typically on the order of 10^{-6} Torr and 10^{-9} Torr, respectively.

2.1.4 Mass Flow Controller

Figure 2.3: The commercial mass flow controller used for our experiment.

We regulated the molecular hydrogen gas flow using a Mass Flow Controller (MFC) [37]. Its rated full-scale flow range is 20 sccm (standard cubic centimeter per minute). We can control the flow rate by supplying a particular setpoint voltage (0 - 5 V) using our electronics as described in section 2.1.6.

We verified the flow rates of the MFC experimentally before installing it in our appara-

tus. For that, we measured the volumetric flow of hydrogen gas through the MFC for a given time at different setpoint voltages. The output gas from the MFC was collected in a measuring cylinder immersed in water. The volume of the gas collected in the cylinder for a given time gives the flow rate. Figure 2.4 presents the flow rates measured in the lab (non-standard temperature and pressure) at various setpoint voltages.

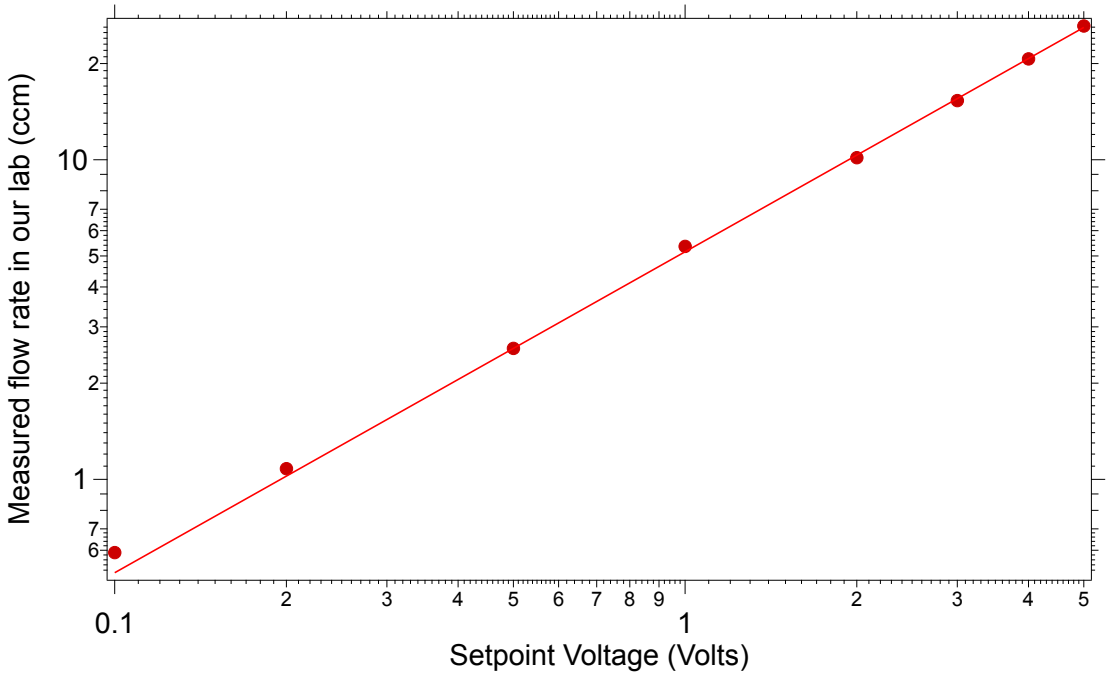

Figure 2.4: The experimentally observed flow rate (in cubic centimetres per minute) plotted against the setpoint voltage (in volts). The data are fitted into a line (y=a+bx) with a = 0 sccm and b = 5.2 sccm/volt.

Conversion of cubic centimetres per minute in our lab to standard cubic centimetres per minute (sccm)

Standard cubic centimetres per minute (sccm) is a unit of flow rate defined at standard temperature and pressure (STP) of 20°C (293 K)and 1 atm (760 Torr) respectively. However, the atmospheric pressure in our lab as measured by the MKS pressure sensor is ∼645 Torr. To establish the relationship between standard cubic centimetres per minute (sccm) and the measurements in our lab, we compare the volume of gas at

standard conditions to 1 cc volume of gas in our lab.

We have,

Pressure in lab $(P_{lab}) = 645$ Torr,

Temperature in lab $(T_{lab}) = 296$ K,

Volume in lab $(V_{lab}) = V_{lab}$,

Pressure at standard conditions $(P_{standard}) = 760$ Torr,

Temperature at standard conditions $(T_{standard}) = 293$ K,

Volume at standard conditions $(V_{standard}) = ?$

Using the ideal gas law:

$$\frac{P_{lab}V_{lab}}{T_{lab}} = \frac{P_{standard}V_{standard}}{T_{standard}}$$

$$\implies V_{standard} = \frac{645 \text{ Torr} \times V_{lab} \times 293 \text{ K}}{760 \text{ Torr} \times 296 \text{ K}}$$

$$\implies V_{standard} = 0.84\ V_{lab}$$

So, 1 cubic centimetres per minute at our lab = 0.84 standard cubic centimetres per minute (sccm).

We used this conversion factor to convert the flow rate measured in our lab to the standard unit– sccm. Figure 2.5 presents the correspondence of standard flow rates to various setpoint voltages.

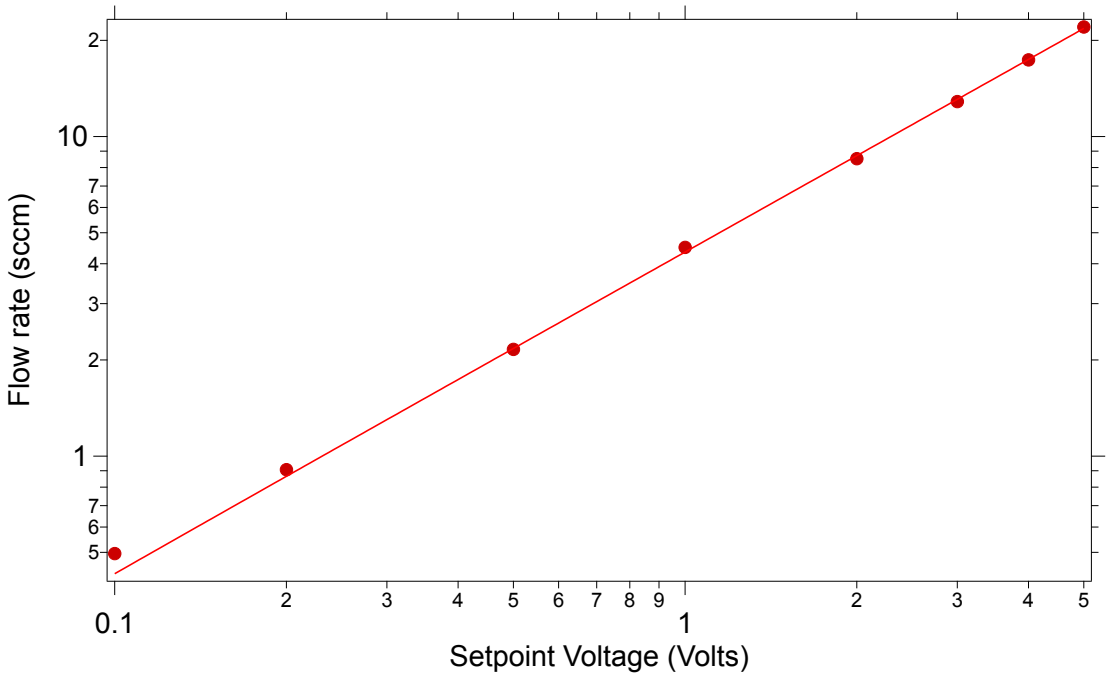

Figure 2.5: The standard flow rate (in standard cubic centimetres per minute) plotted against the setpoint voltage (in volts). The data are fitted into a line (y=a+bx) with a = 0 sccm and b = 4.36 sccm/volt.

2.1.5 Spectroscopy

We performed absorption spectroscopy using a commercial Fourier-transform infrared FTIR spectrometer— Thermo Fisher Nicolet iS50 FT-IR. The spectrometer has IR and white light sources; we used the white light source because it has higher intensity at the wavenumbers of interest in our experiment: ∼4000 to ∼5000 cm^{-1}.

This white light from the spectrometer is guided through the sample using a series of mirrors. A plano-convex lens [38] of focal length 500 mm is placed in the FTIR optical path before the cryostat to focus the beam reaching the sample. The beam size at the sample is 4 mm by 5 mm (FWHM). The light transmitted through the sample is focused into an external mercury cadmium telluride (MCT) detector using a parabolic mirror. The detector is cooled using liquid nitrogen during its operation. To run the scans, we used the settings of gain: 4, optical velocity: 1.8988, aperture: 1, resolution: 0.125

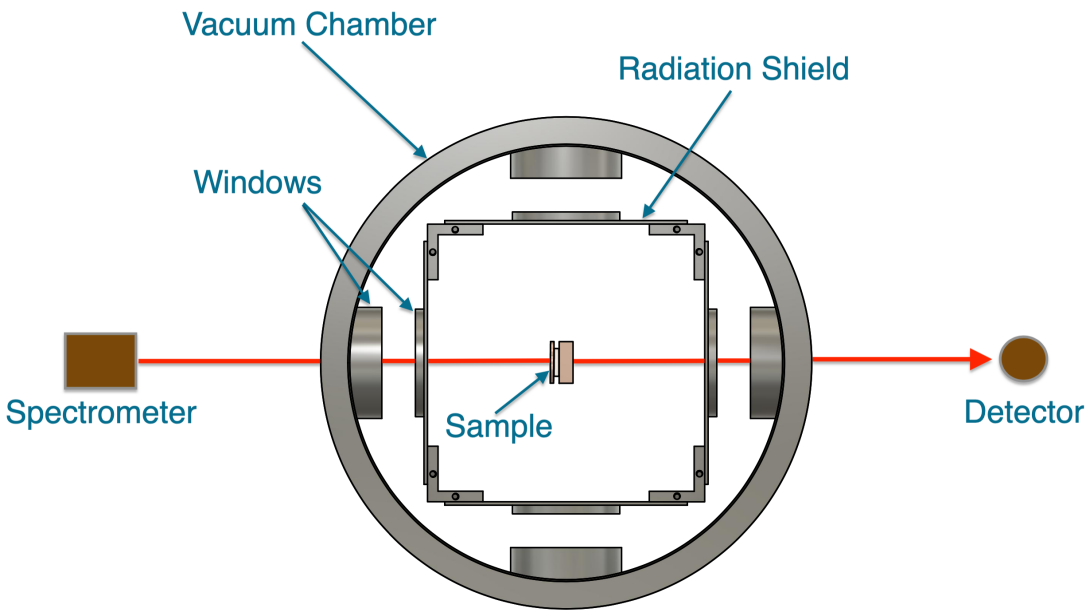

Figure 2.6: Schematic for the FTIR beam path (bottom view of the chamber).

cm^{-1}, and range: 200-10000 cm^{-1}.

2.1.6 Electronics box

We built an electronics box for powering the temperature sensors and logging the voltage drop across them. We designed a printed circuit board (PCB) that consisted of one voltage regulating circuit and six current regulating circuits as shown in the figure 2.7. The circuit diagram for the PCB is shown in figure 2.8.

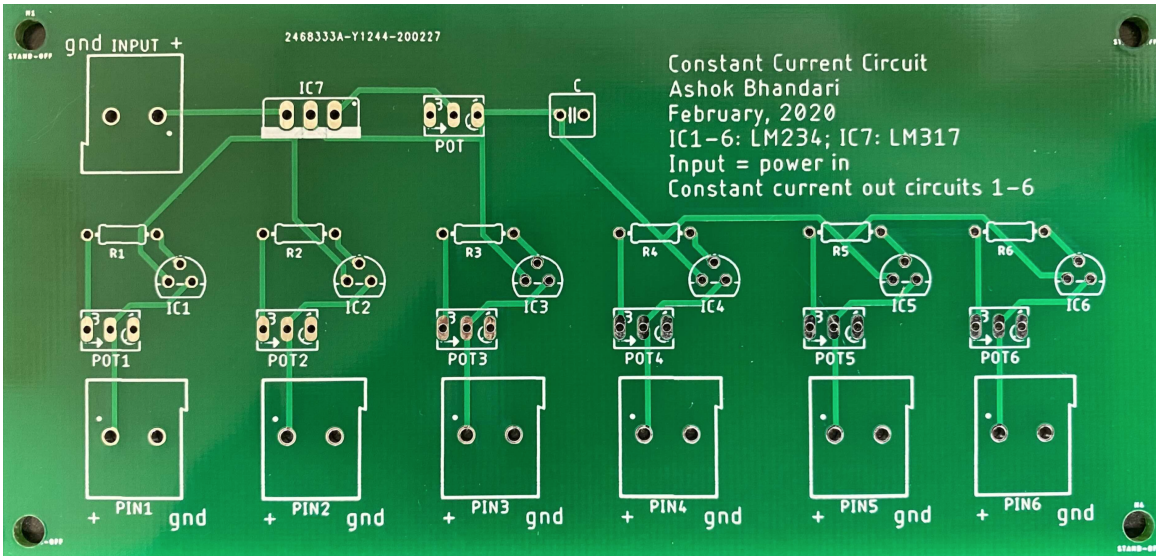

Figure 2.7: The printed circuit board used in the electronics box. In this PCB, there are six current regulating circuits and one voltage regulating circuit.

For voltage regulation, we used a LM317 transistor [39]. The voltage regulating circuit consists of the transistor along with an adjustable potentiometer and a capacitor. The output voltage from the voltage regulating circuit is given by:

$$V_{out} = 1.25 \times (1 + \frac{R_2}{R_1}) \tag{2.1}$$

Here, the ratio of R_1 and R_2 was adjusted using the potentiometer to obtain the constant output voltage of 9 V. The capacitor with capacitance 47 μF was used to improve the transient response.

For the current regulation, we used a 3-terminal adjustable current source (LM234)

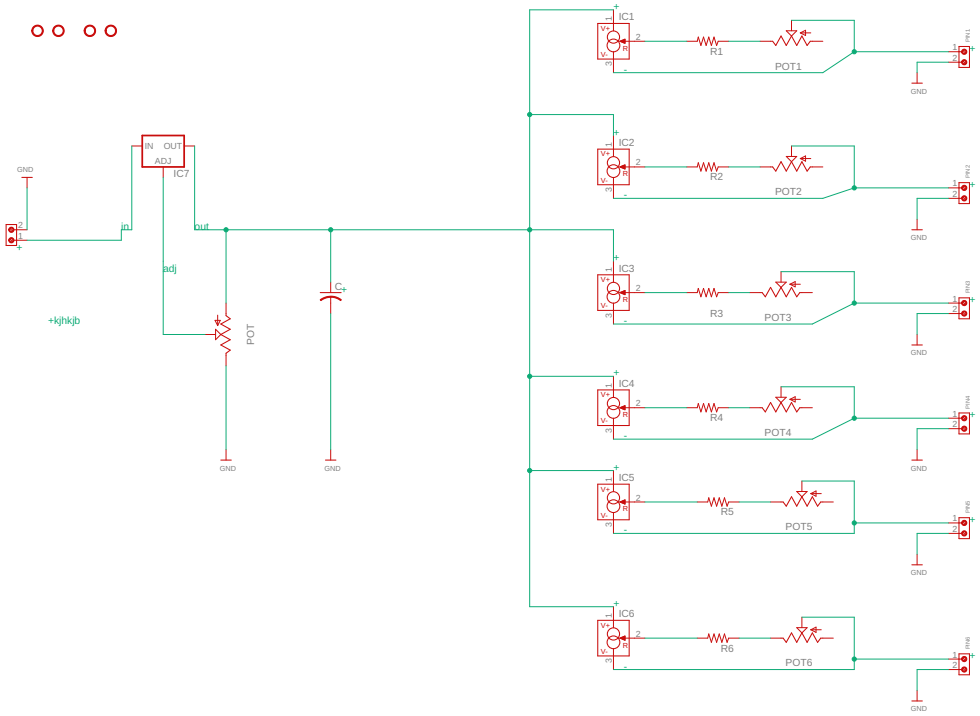

Figure 2.8: Circuit diagram for voltage regulating circuit and current regulating circuits in the PCB.

from Texas Instruments [40]. Figure 2.9 is the typical performance characteristics plot of set current with respect to the turn-on voltage for LM234 [40]. According to figure 2.9, using a R_{total} of 6.8 kΩ with sufficient turn-on voltage is required to obtain the output current of 10 μA.

We used a resistor of resistance 6.5 kΩ and an adjustable potentiometer along with the current regulator to complete each current regulating circuits. The turn-on voltage is supplied by the output voltage from the voltage regulating circuit. We adjusted the resistance from the potentiometer to obtain the required output current.

When we power the temperature sensors, there is a voltage drop across them. We used

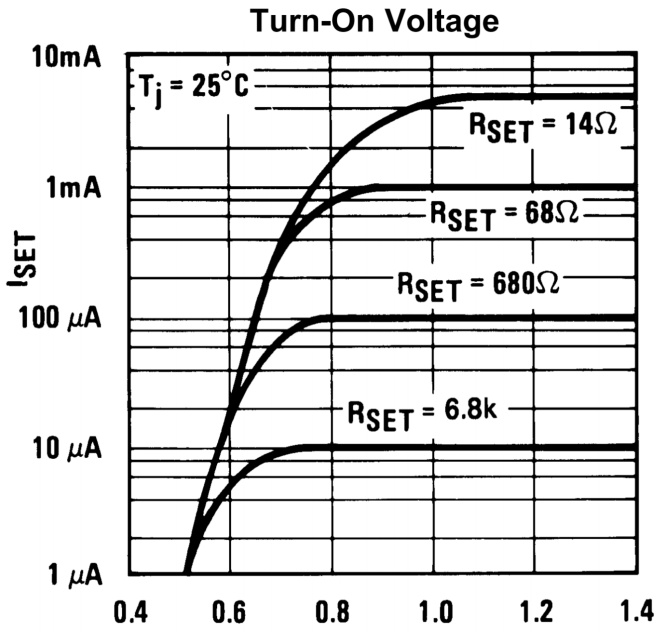

Figure 2.9: The typical performance characteristics plot of set current with respect to the turn-on voltage for LM234. The figure is reproduced from reference [40].

those voltages as the analog inputs for the LabVIEW board in the computer [41]. To connect the sensor voltages to the borad we used a connector block [42] in our electronics box, as shown in figure 2.10. We also used the analog voltage output channel of the LabVIEW board to control the setpoint voltage for the Mass Flow Controller (MFC).

Along with the temperature sensors, we supply 15 V power to the MKS pressure sensor and the mass flow controller using our electronics box. We monitored and logged the temperature, pressure, and MFC setpoint voltage data using the LabVIEW program as discussed in Section 2.4. The electronics box including all of its components discussed above is presented in figure 2.10. One of the BNC connectors in the electronics box is used for supplying power to the heater placed on the second stage OP converter, while rest of them are currently not connected to anything– we can make those connections as per our future requirements. The military connection cable makes electrical connection between the sensors inside the vacuum chamber and the electronics box. This cable connects to the electrical feedthrough on the top of the vacuum chamber. The “power

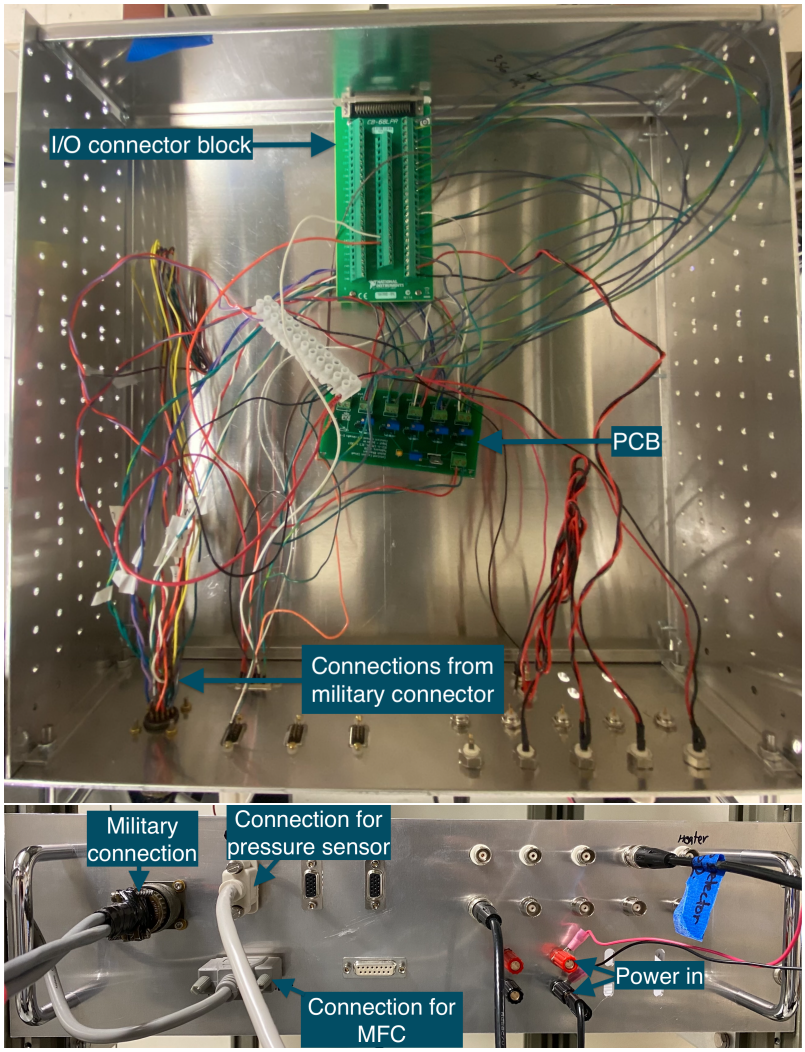

Figure 2.10: The inside and outside view of the electronics box.

in" connections are connected to the DC power source of ~15 V.

2.2 Cryogenic parts

2.2.1 Cryocooler

We used a Cryomech PT-415 pulse-tube cooler for cooling our cryostat [43]. This cryocooler has two stages: the first stage and the second stage. The first stage reaches a base temperature of 31 K, whereas the second stage reaches a base temperature of 2.8 K with no heat load. The cooling capacity for the first stage is 45 W at 45 K and that for the second stage is 1.5 W at 4.2 K. Figure 2.11 shows the capacity curve for our cryocooler.

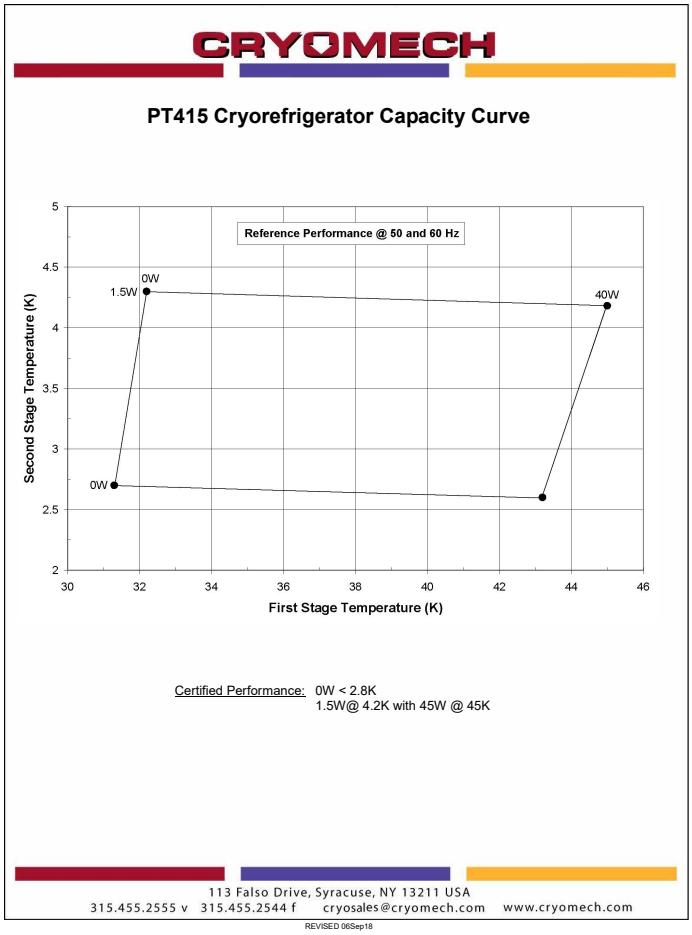

Figure 2.11: The capacity curve for PT-415 Cryorefrigerator reproduced from reference [43].

2.2.2 OP converters

There are two “OP converters" (ortho–para converters) used in our experiment. We made the OP converters using ¼" copper "refrigerator tubing" made of alloy 122, which is filled with the catalyst (explained in section 2.3). Before being filled with catalyst, each copper tube is soldered into a 1/4"-diameter through-hole in a copper block using Stay-Brite solder for a thermal and mechanical connection, as shown in figure 2.12. The through-hole in the copper block is 0.5" long in the case of the first-stage OP converter

and 1" long in the case of the second-stage OP converter. After filling the copper tubing with the catalyst, the glass wool is inserted in the tubes so as to prevent spilling of granular catalyst. The Swagelok-style compression fittings used to join the different parts of our hydrogen gas “plumbing” keep the glass wool in place. The copper mount of OP converters are connected to different parts of the cryostat. The length of the second stage and the first stage OP converter tubings are $\sim$ 16 inches and $\sim$ 12 inches respectively.

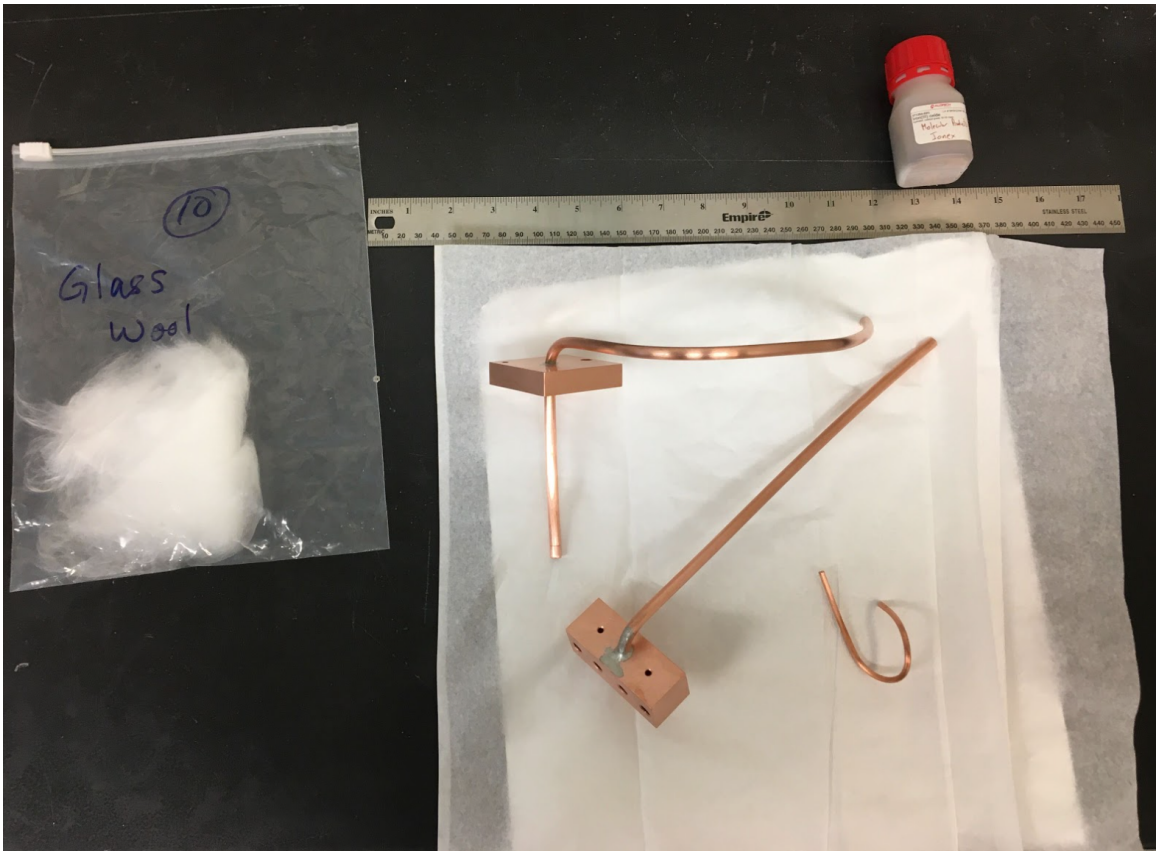

Figure 2.12: The first and the second stage OP converters, along with the bottle of catalyst and glass wool before anchoring them to the cryostat.

We thermally anchored the first stage OP mount to the first stage cold plate as shown in figure 2.1. During hydrogen flow, its temperature is 42.5 $\pm$ 2.5 K. The second stage OP mount is suspended from the bottom of the cold finger plate using a few 4" threaded 1/4-20 brass rods (as discussed in section 2.2.5). Since the thermal equilibrium ortho

fraction depends on the temperature of the catalyst, we want to operate our OP converter at a range of temperatures. The number of rods used can be changed to obtain the desired thermal conductance between them. We secured the rods with nuts and washers on both sides of the cold finger plate and the second stage OP mount such that the distance between the top of the second stage OP mount and the bottom of the cold finger plate is 5 cm. The distance from the bottom of the first stage OP converter fitting to the top of the second stage OP converter fitting is 12.5 inches. The temperature of second stage OP converter can be controlled using the heater [44] that is mounted on the OP block. The temperature of second stage OP converter is monitored with a help of silicon diode sensor mounted on the OP block.

We have used two OP converters in our experiment. While most of the OP conversion is performed by the second stage OP converter, the first stage OP converter pre-cools the incoming gas from the room temperature before reaching the second stage OP converter, and thus lowering the thermal load on the second stage OP converter. Now onwards, the second stage OP converter shall be referred to as the "OP converter" throughout this thesis.

2.2.3 Cold Finger

The cold finger is a copper block (alloy 101 or 110) of dimension 4.5" × 1.5" × 0.5" with a hole of diameter 0.5" on it. The detailed machine drawing for the cold finger is available in appendix A. The cold finger is attached to the cold finger plate using two ¼-20 Brass Hex screws such that it hangs down the plate perpendicularly as shown in figure 2.13. We apply a thin layer of Apiezon N grease in the junction between the cold finger and the cold finger plate.

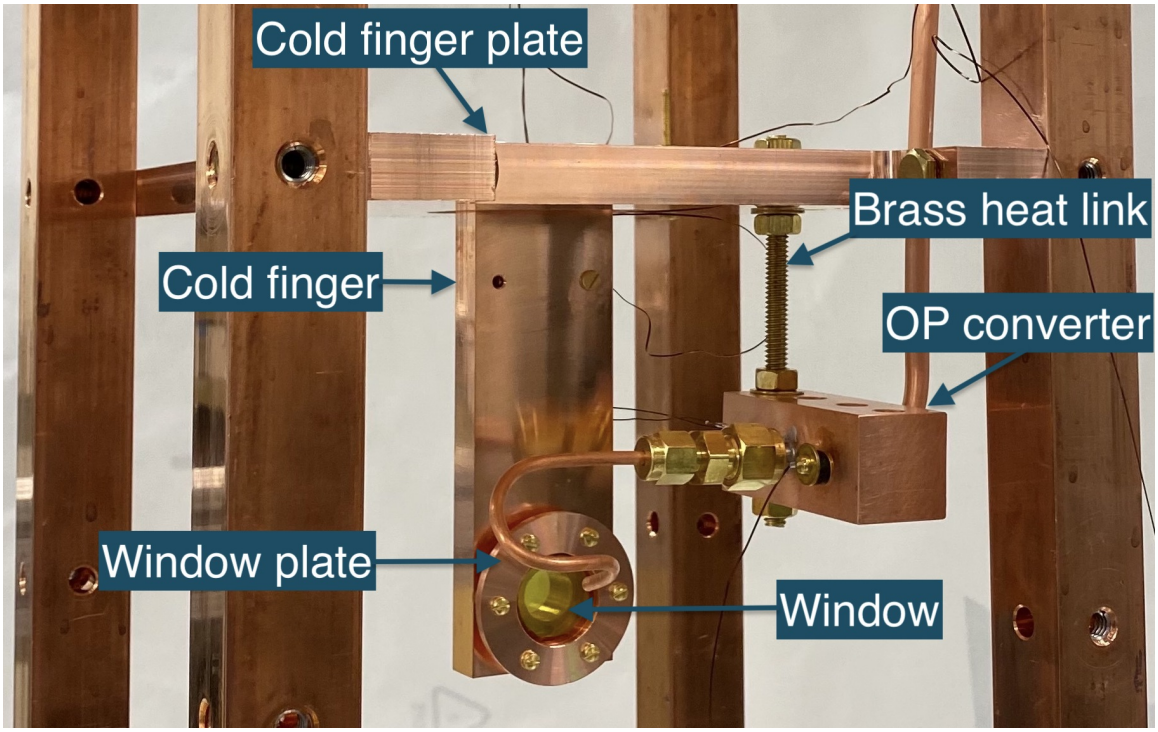

Figure 2.13: The “heart” of our apparatus. Omitted from the schematic are the surrounding radiation shield and vacuum chamber. All parts shown are copper, with the exception of the brass hardware and the sapphire window. The structural components are copper alloys 101 and 110; the copper tubing is alloy 122.

2.2.4 Substrate

We deposited the parahydrogen gas on the transparent sapphire window. It is an anti-reflection coated sapphire wedged window [45] of diameter 1" and thickness of 5 mm, and has a wedge angle of 30 ± 10 arcmins. The sapphire window is placed in alignment with the 0.5" hole in the cold finger and is secured in place with the help of a window plate. The window plate is a copper ring 0.125" thick with an inner diameter of 0.75" and an outer diameter of 1.5". The detailed machine drawing for the window plate is available in appendix A. The sapphire window is thermally connected to the cold finger using indium. The window plate secured the sapphire window in place with 4-40 brass screws. A kapton ring of thickness 0.005" is placed in between the sapphire window and the window plate to avoid possible cracking from direct window-to-metal contact.

2.2.5 Heat Links

Heat links for cold-finger

Due to the chamber's geometry, the lowest end of the cold finger is 21" below the cryocooler's second stage. We have thermally linked the second-stage cryocooler to the cold finger via flexible and rigid copper heat links. The flexible heat links are made of copper wires provided with copper brackets for thermal contact. The details about the flexible heat links are available in Kyle Hardman's thesis [31]. The rigid copper links consist of copper plates (4 K plate & cold finger plate) and copper frame as shown in figure 2.1.

The copper 4 K plate is thermally connected to the cryocooler second stage using four flexible heat links. The 4 K plate is attached to the 4 K frame which connects to the cold finger plate. The four copper blocks, each of dimension 25" X 1" X 1" that runs vertically downwards from the 4 K plate, make the 4 K frame. A "Cold Finger Plate" made of copper (alloy 101 or 110) is attached to the 4K frame using four ¼-20 Brass Hex screws such that the distance between the second stage cryocooler and the cold finger plate is 16.4". The measured thermal resistance between the cryocooler and the cold finger is 4.3 K/W at 4 K. This is significant compared to the cryocooler's effective resistance (1 K/W). However, we can improve this in our future versions.

Heat links for OP converter

The first stage OP mount is bolted on the first stage cold plate using single ¼-20 Brass Hex screw and lock washer. The second stage OP mount is thermally linked to the cold finger plate using a few ¼-20 threaded brass rods as shown in figure 2.13. These brass rods are 0.1 m long. We can change the number of brass rods to vary the conductivity of the heat link such that the second stage OP converter is maintained at elevated tem-

peratures without significant thermal load to the cold finger plate. With this setup, we can operate the second-stage OP converter within the 8 K to 30 K temperature range.

We performed the experiment using three configurations of the heat links. We performed the growths for OP converter temperature < 15 K by thermally connecting the cold finger plate with the second stage OP mount using three brass rods. We used two brass rods as thermal link for the intermediate growths (15 K to 21 K) and a single brass rod for the hotter growths (21 K to 30 K).

2.2.6 Hydrogen Plumbing

The plumbing for the hydrogen gas flowing inside the chamber is shown in figure 2.1. The hydrogen gas flows into the vacuum chamber via mass flow controller (MFC). A flexible stainless steel tubing [46] connects the output channel from MFC to the room-temperature-end of the vaccum feedthrough, and the vacuum-end of the feedthrough to the first stage OP converter. The connections are made using VCRs and Swageloks. We bent a 29" long smooth-bore seamless stainless steel tubing [47] into coils (like a spring) for flexibility and connected it to the copper tubings of the first and second stage OP converter. The connections are made using using ¼" to 1/16" stainless steel straight reducers [48]. The other end of the second stage OP converter that runs towards the cold finger is provided with a brass ¼" to 1/8" parker compression fitting. The 1/8" copper tubing is fitted to the other end of this brass parker compression fitting and is bent in such a way that it deposits the hydrogen gas to the window as shown in figure 2.13. The end of this 1/8" copper tubing is approximately 3 cm away from the sapphire window.

2.3 Catalyst

We used the Molecular Products Ionex OP catalyst for the effective conversion of ortho hydrogen to para hydrogen. We used a bottle of Aldrich 371254-50G Iron (III) oxide hydrated, catalyst grade 30-50 mesh (Lot #MKBQ2447V) as the catalyst. We filled ~ 9 grams and ~ 7 grams of catalyst respectively into the first and second stage OP tubings (explained in section 2.2.2).

2.4 Data acquisition and analysis

We acquired the real-time data for cryostat temperatures, and the chamber pressure through the LabVIEW program [49]. We used IGOR Pro software for the data analysis [50]. IGOR can be programmed to load the data, display it and perform various statistical calculations.

Chapter 3

Experimental Setup and Sample growth

3.1 Experimental setup and growth conditions

The cooldown curve of the cryostat is presented in figure 3.1. It takes $\sim$ 15 hours for the parts inside the vaccum chamber to reach to their base temperatures. The base temperatures for first stage cold plate, cold finger plate, cold finger and cryocooler second stage are $\sim$ 42 K, $\sim$ 4 K, $\sim$ 3.6 K and $\sim$ 2.7 K respectively. It should be noted that the cold finger is thermally linked to second stage of cryocooler via cold finger plate; the temperature of the cold finger should be higher than that of the cold finger plate. However, figure 3.1 shows that the cold finger is colder than the cold finger plate. This is because the silicon diode temperature sensors used for measuring these temperatures have a tolerance of $\pm$ 0.5 K (described in section 2.1.2).

The base temperature of OP converter depends on the number of brass heat links chosen (as described in section 2.2.5). For the cooldown data presented in figure 3.1, the base

temperature of OP converter is $\sim$ 11 K, which is obtained using a single brass heat link.

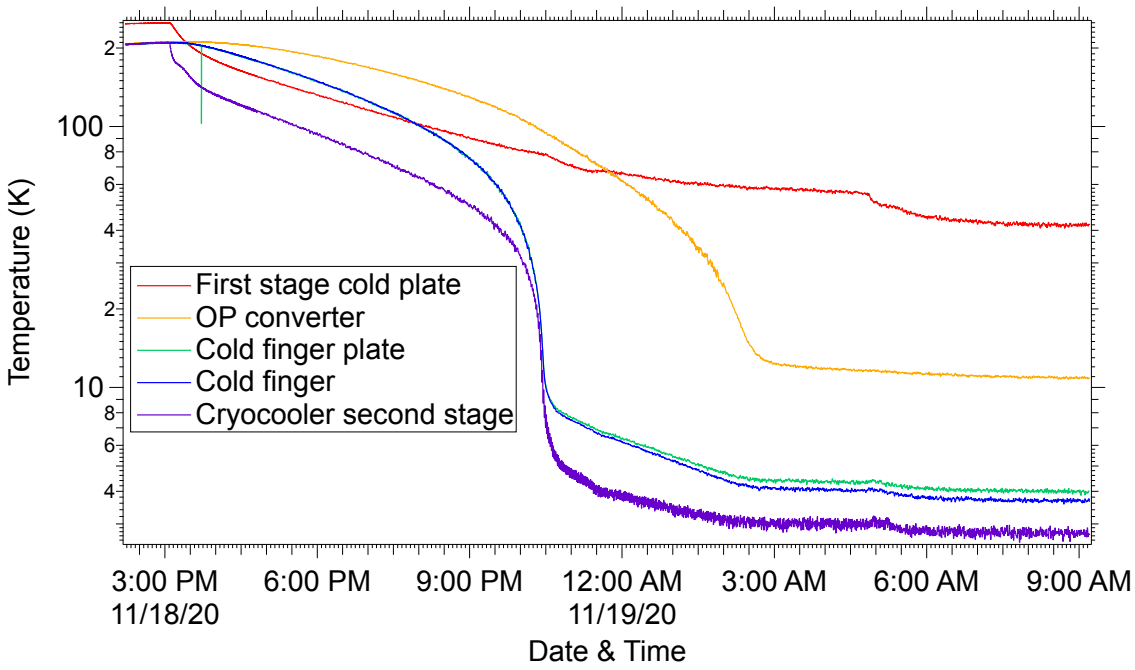

Figure 3.1: The cooldown curve of the cryostat.

We used vapor deposition technique to grow high-purity parahydrogen samples [24, 27, 28]. A mass flow controller (MFC), mounted on the top of the chamber at room temperature, regulates the flow rate of 4 sccm. The hydrogen gas passes into the cryostat following the gas line described in section 2.2.6. The gas is cooled in two stages in two OP converters. The details about OP converters are discussed in section 2.2.2. The first stage OP converter is thermally connected to first stage of pulsed tube cryocooler. This stage has a large cooling power and works well for the large thermal load due to incoming gas beam from room temperature. The second stage OP converter is thermally anchored to cold finger plate using 1/4-20 brass rods as explained in section 2.2.5. The thermal equilibrium ortho fraction for the parahydrogen samples grown using this setup should correspond to the temperature of the catalyst in the second stage OP converter.

We monitor the sample thickness using FTIR spectroscopy. This spectroscopic technique is used after sample growth to measure the sample's orthohydrogen fraction, as

discussed in section 4. Sample thicknesses ranged from 0.4 to 4 mm; deposition rates are discussed in section 5.1. Samples were grown for second-stage OP converter temperatures ranging from 8.1 K to 29 K.

The temperature profile of the cryostat during sample growth is shown in figure 3.2. At timestamp 10:49 AM, we supplied power to heater on the OP converter, and at 12:20 PM, we initiated the flow from the MFC. The deposition began at 1:50 PM. We stopped the sample growth at 8:00 PM by turning off the MFC.

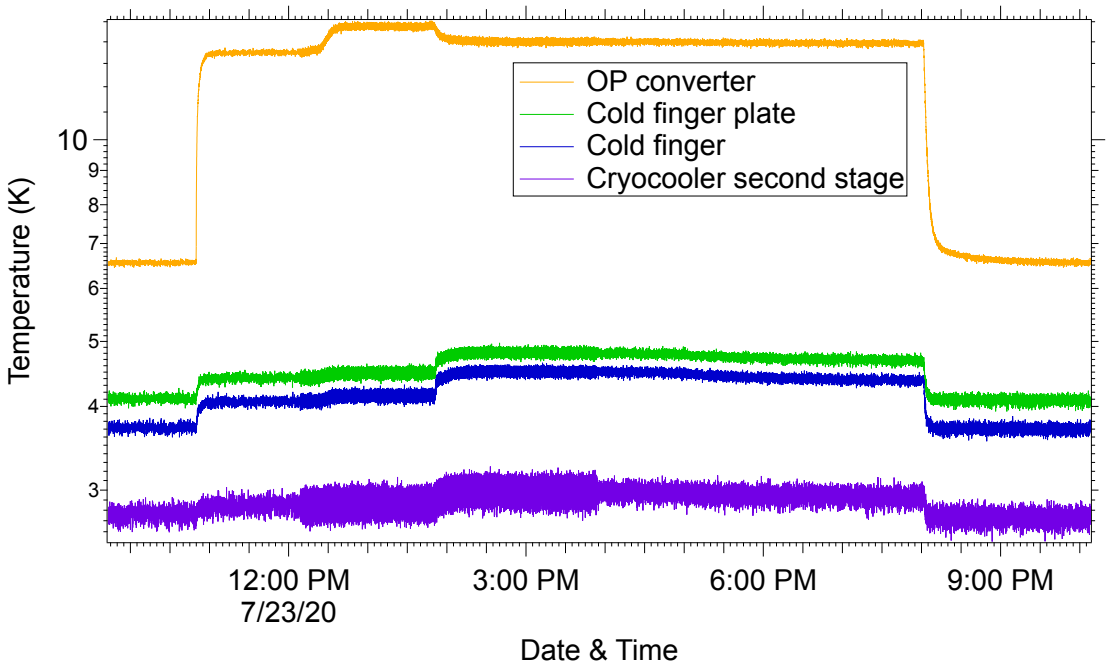

Figure 3.2: The temperature profile of the cryostat during sample growth. The temperature of the first stage cold plate (which is not presented in the graph above) is consistent around 42.5 ± 0.2 K.

During sample growth, the cold finger temperature ranged from 3.8 K to 4.6 K, up from its base temperature due to the heat load from depositing gas and the heater used to maintain the OP converter at elevated temperatures. We observed a delay in deposition of hydrogen onto the substrate (explained in section 3.3). During the delay, the heat load on the OP converter from the gas is greater than the heat load after the deposition

begins as shown in figure 3.2.

3.2 Chamber Pressure

We performed the RGA pressure measurements before each sample growth to measure the background vacuum. The typical ion-gauge readouts of the background vacuum were on the order of 10^{-8} Torr. The partial pressure of H_2 was typically on the order of 10^{-9} Torr, and that of He is $< 10^{-10}$ Torr. During the sample growths, we kept the turbo-pump running, and the chamber pressures were on the order of 10^{-7} Torr. During the sample growth, the partial pressures of H_2 and He are typically on the order of 10^{-6} Torr and 10^{-9} Torr, respectively.

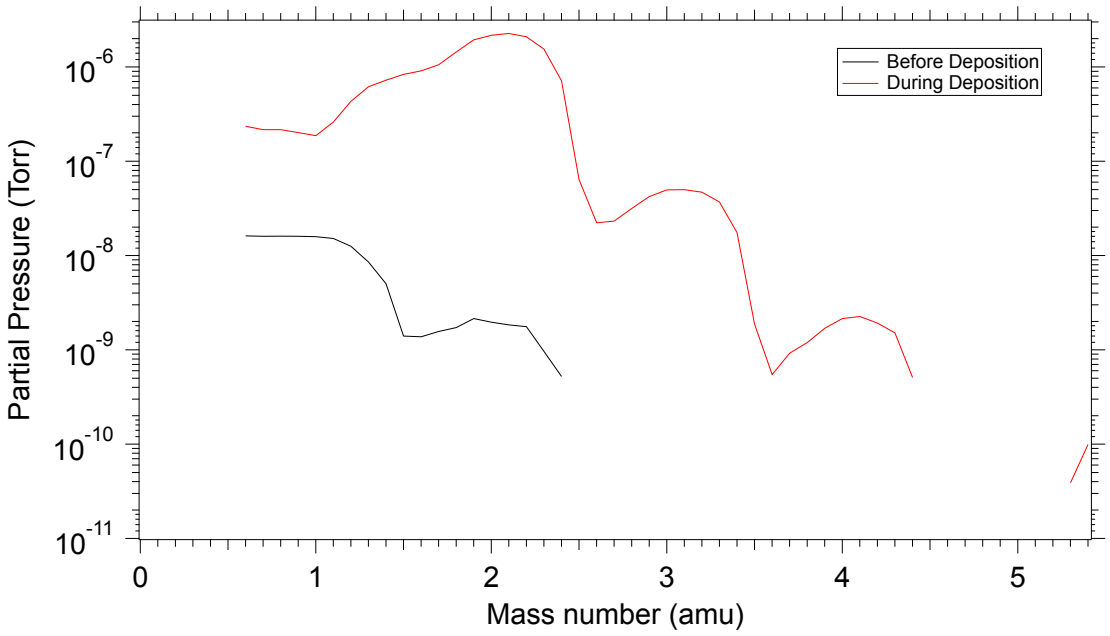

Figure 3.3: The partial pressure inside the chamber recorded by the RGA, plotted as a function of the mass number for our highest OP converter temperature growth (∼28 K).

3.3 Delay in Deposition

In our sample growth experiments, we observed a significant delay between the start of the hydrogen flow at the room-temperature mass-flow controller and the beginning of sample growth. We attribute the delay to the adsorption of hydrogen molecules onto the surface of the catalyst. Once this layer reaches a "saturation" thickness, hydrogen exits the OP converter. We attribute the extra heat load during deposition to the sum of the heat load of cooling the incoming gas (which is also present during steady-state flow) and the heat of deposition (which goes to zero during steady-state flow).

Figure 3.4 shows the delay time between the start of hydrogen gas flow and the beginning of sample growth, plotted as a function of the average temperature of the second-stage OP converter during the delay. The delay for flow rates of 4 and 17 sccm both are included in the plot. The detailed discussion on the sample growths at higher flow rates can be found in section 6. For the similar OP converter temperatures, we observed that the delay time at 17 sccm flow rate is roughly 4 times smaller than the delay time at 4 sccm.

In order to estimate the monolayers of adsorbed H_2 solid on the surface of the OP catalyst, we perform the following calculation:

Standard cubic centimetres per minute (sccm) is a volumetric unit of flow rate defined at standard temperature and pressure (STP) of 20°C and 1 atm respectively.

Using the ideal gas law, we get,

$$1 \text{ sccm} \equiv 2.69 \times 10^{19} \frac{\text{molecules}}{\text{minute}}$$

We used this conversion factor to calculate ∼4 sccm hydrogen gas flow rate into the chamber. The number of molecules adsorbed is quantified using the time delay (figure

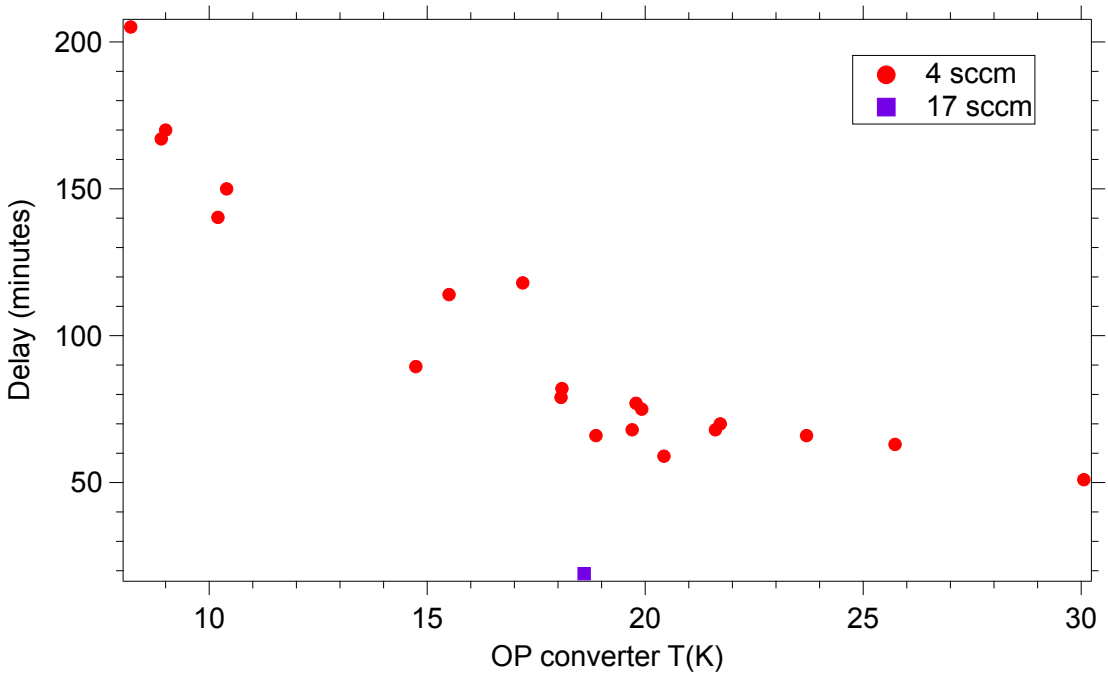

Figure 3.4: The delay time between the start of hydrogen gas flow and the beginning of sample growth, plotted as a function of the average temperature of the second-stage OP converter during the delay. The delay for flow rates of 4 and 17 sccm both are presented in the plot.

3.4) and the flow rate. The number of molecules adsorbed on the surface of the catalyst in the second stage OP converter exhibits decreasing trend on increasing the catalyst temperature and is independent to the flow rates as shown in figure 3.5.

We further estimated the thickness of the adsorbed layer using the prior surface area measurements of the catalyst [51], and by approximating the density of a thin film of hydrogen to be the same as the bulk density [12]. From this model, and the assumption that the hydrogen is deposited primarily in the second-stage OP converter, the observed delay at our coldest OP temperatures corresponds to a deposited hydrogen film ~ 2 monolayers thick, and the delay at OP converter temperature of 30 K would correspond to a half-monolayer-thick film. Figure 3.6 shows number of monolayers deposited on the catalyst surface, plotted as a function of the average temperature of the second-stage OP converter during the deposition. It shows that the number of monolayers deposited

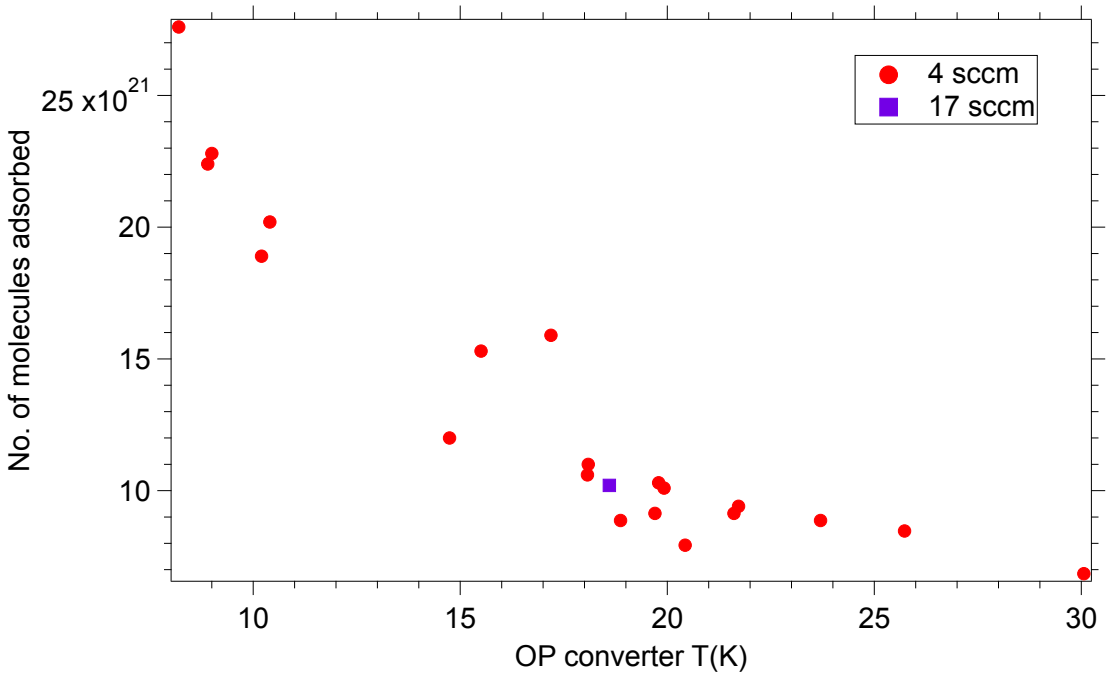

Figure 3.5: The number of molecules adsorbed on the catalyst surface, plotted as a function of the average temperature of the second-stage OP converter during the deposition.

in the surface of the catalyst is consistent with the OP converter temperature and is independent of the flow rate.

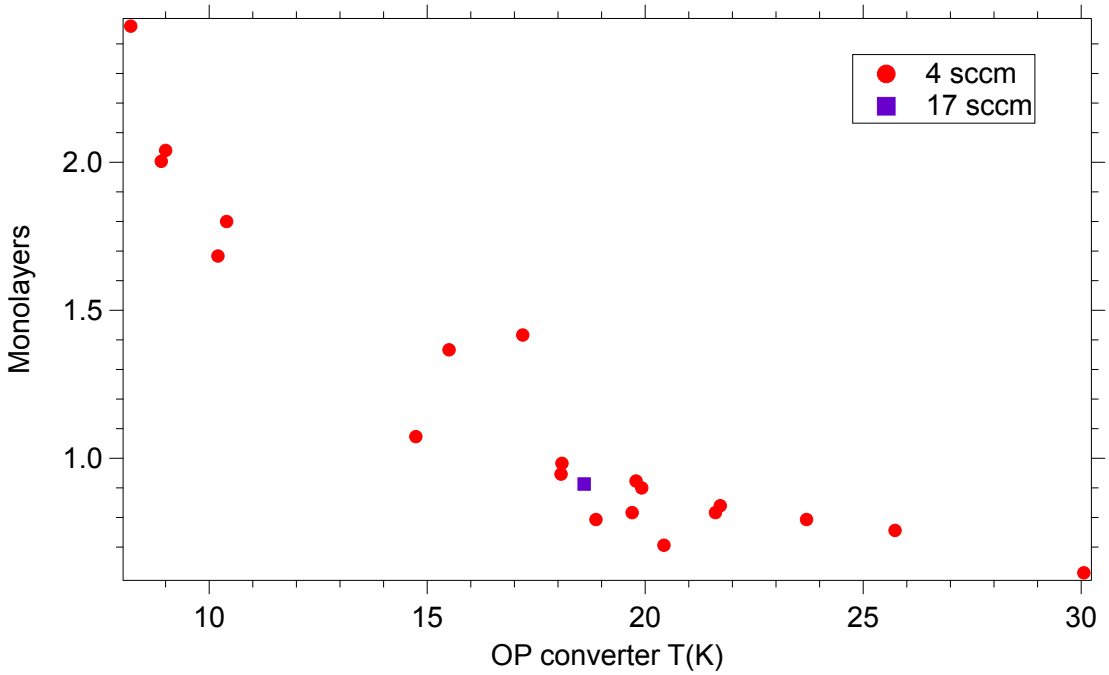

Figure 3.6: The number of monolayers deposited on the catalyst surface, plotted as a function of the average temperature of the second-stage OP converter during the deposition. The data for both 4 and 17 sccm flow rates are presented in the plot.

Chapter 4

OD spectrum of Solid Parahydrogen

We take the FTIR spectrum with the hydrogen sample ($I(\nu)$) and without the sample ($I_0(\nu)$) as described in section 2.1.5 . Figure 4.1 presents the comparison of the spectra with and without the sample. The atmospheric absorption lines are dominant in the regions around 4000 cm^{-1}, 5500 cm^{-1} and 7500 cm^{-1} wavenumbers. The spectra with sample (red curve) exhibits additional absorption lines between 4000 cm^{-1} and 5000 cm^{-1} wavenumbers; these are the parahydrogen transitions we are interested in.

We then calculate the transmission of the solid parahydrogen by comparing spectra taken with and without the sample: $T = \left(\frac{I(\nu)}{I_0(\nu)}\right)$. We convert this transmission to an the optical depth (OD) using: $T \equiv e^{-\mathrm{OD}}$.

The FTIR beam passes through the multiple windows in our cryostat, hence producing the interference fringes. This is called etalon effects. In order to remove interference fringes arising due to etalon effects, we filter our OD spectra. For that, we select a region in the OD spectrum where there are no absorption transition features, and take its Fourier transform (magnitude squared) to determine the frequency of the interference fringes. We use a notch filter at those frequencies to filter the OD spectrum. Figure 4.2

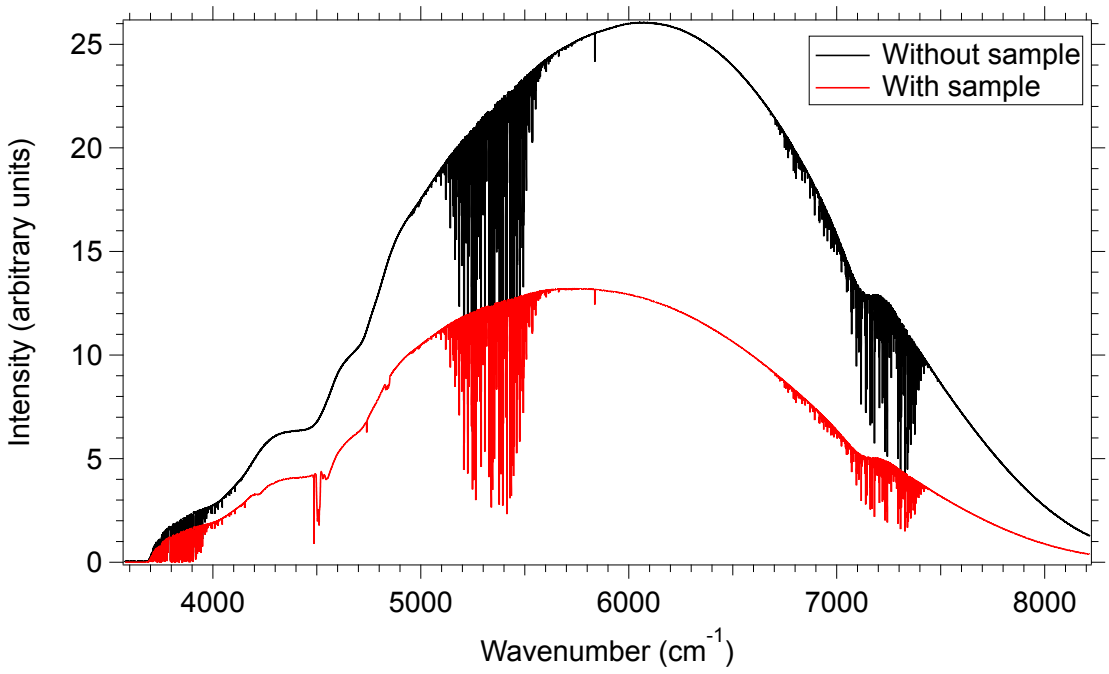

Figure 4.1: The raw absorption spectrum with and without the sample plotted against the wavenumber. We process these spectrum to calculate the optical depth (OD) as described in the text.

shows the comparison between unfiltered and filtered OD spectra around 4740 cm^{-1}. Clearly, the etalon effecs are supressed by filtering the data.

Sample spectra of two parahydrogen samples are shown in figure 4.3, where we have plotted optical depth, OD = -$\log_e\left(\frac{I(\nu)}{I_0(\nu)}\right)$ as a function of wavenumber (cm^{-1}).

In this work, we are dealing with with ro-vibrational transitions. These are the transitions where rotational and vibrational quantum numbers change. These transitions are labeled using the notation:

$$X_a(b)$$

where, $X : \Delta J = J_{\text{final}} - J_{\text{initial}}$,

a : the excited state vibrational level (denoted by integers), and

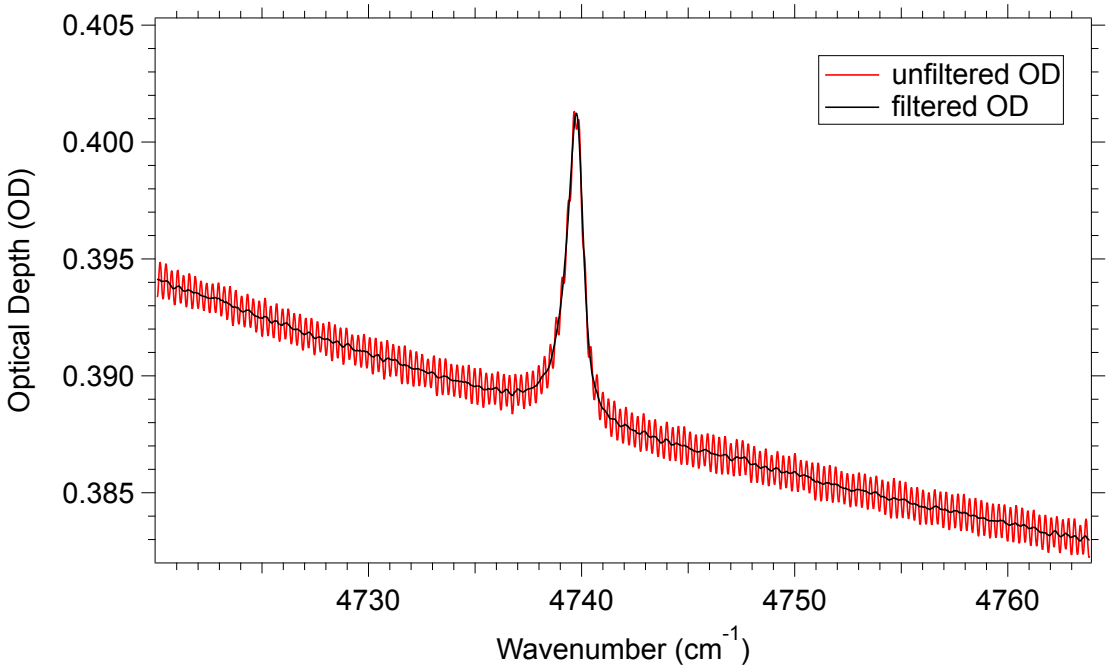

Figure 4.2: The unfiltered and the filtered OD curve for a given sample (grown at OP converter 20 K) plotted against the wavenumber. The OD curve is filtered as described in the text.

b : the initial rotational state denoted by J_{initial}.

Note that all lines originate in $a = 0$ vibrational state. The frequently encountered ΔJ values and their corresponding symbol are listed in the table below.

X	P	Q	R	S	U
ΔJ	-1	0	+1	+2	+4

The table 4.1 consists of the list of spectral features in solid hydrogen encountered in this work. The transitions are labeled either in a single $X_a(b)$ or in a double $X_a(b)$ + $Y_c(d)$ notation. The single transition notation corresponds to excitation in a single parahydrogen molecule or orthohydrogen molecule whereas the double transition notation represents the simultaneous excitation of two neighbouring molecules [20]. These labels are consistent with the notation used in references [52, 53, 54].

Transition	Wavenumber (cm^{-1})	Notes
$Q_1(0) + S_0(0)$	4495 - 4520	Broad feature: excitation in the two neighbouring parahydrogen molecules
$S_1(0) + S_0(0)$	4825 - 4855	Broad feature: excitation in the two neighbouring parahydrogen molecules
$Q_1(0) + Q_0(1)$	4153	Vibrational transition in a parahydrogen molecule ($Q_1(0)$) and an orientational transition in a neighbouring orthohydrogen molecule($Q_0(1)$)
$Q_1(0) + S_0(1)$	4740	Vibrational transition in a parahydrohen molecule ($Q_1(0)$) and a rotational transition in a neighbouring orthohydrogen molecule($S_0(1)$)
$Q_1(0)_{H_2} + S_0(0)_{HD}$	4420	Vibrational transition in a parahydrogen molecule ($Q_1(0)_{H_2}$)) and rotational transition in a neighbouring HD molecule ($S_0(0)_{HD}$)

Table 4.1: A list of single and double IR transitions in solid hydrogen. The labels of these spectral features are consistent with the notation used in references [52, 53, 54].

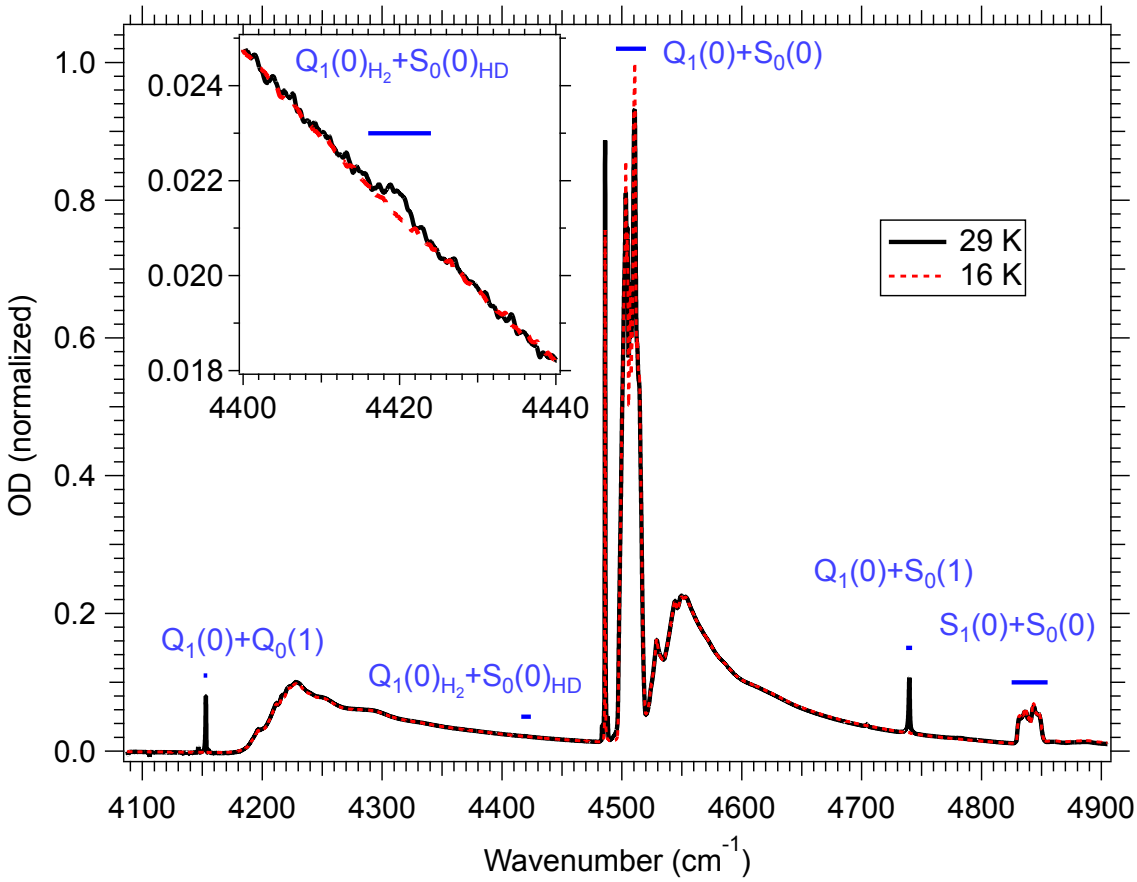

Figure 4.3: Spectra of two samples grown at OP converter temperatures of 16 and 29 K. To simplify visual comparison of the two spectra, the background OD has been subtracted, the spectra have been normalized by the area of the $Q_1(0)+S_0(0)$ transition, and the spectra have been low-pass filtered to reduce the resolution to ~ 0.5 cm^{-1}. These operations are not done on the spectra used for analysis of our samples. The spectral features used in this paper are labeled according to the notation of references [52, 53, 54]. The inset shows the same spectrum as the main figure, "zoomed in" to show the transition used to measure HD molecules.

4.1 Measurement of sample thickness

We determine the thickness t of the sample using the $Q_1(0) + S_0(0)$ and $S_1(0) + S_0(0)$ transitions, following the procedure outlined by Fajardo [52].

$$t = 4.8 \times 10^{-2}\ \text{mm} \cdot \int_{4495\ \text{cm}^{-1}}^{4520\ \text{cm}^{-1}} \text{OD}\, d\text{n}/\text{cm}^{-1} \tag{4.1}$$

$$t = 6.2 \times 10^{-1}\ \text{mm} \cdot \int_{4825\ \text{cm}^{-1}}^{4855\ \text{cm}^{-1}} \text{OD}\, d\text{n}/\text{cm}^{-1} \tag{4.2}$$

In both equations 4.1 and 4.2, the background OD is subtracted from the integral under the assumption that it is equal to a linear interpolation of the OD at the endpoints of the integral, as per reference [52]. The estimated thickness error for these formulae is ±3% in the limit of low orthohydrogen fraction [52]. For our data, we find the two transitions give similar values of t, with a standard deviation of 1.3%.

For our further calculations, we use the average thickness from these two thickness measurements.

4.2 Measurement of ortho fraction

For the experimental determination of the equilibrium ortho fraction, we use various absorption features in the OD curve. As seen in figure 4.3, the optical depths of the $Q_1(0) + Q_0(1)$ and $Q_1(0) + S_0(1)$ "ortho-induced" transitions (at 4150 and 4740 cm^{-1}, respectviely) depend on the orthohydrogen fraction in the sample. The dependence of the $Q_1(0) + Q_0(1)$ transition's optical depth on the orthohydrogen fraction f_{ortho} has previously been reported in the literature. In the low-ortho limit, Fajardo [55] reports

that:

$$f_{\text{ortho}} = \frac{1.24 \times 10^{-1}\ \text{mm}}{t} \cdot \int_{4151\ \text{cm}^{-1}}^{4154\ \text{cm}^{-1}} \text{OD}\, d\text{n/cm}^{-1} \tag{4.3}$$

with the background OD subtracted from the integral under the assumption that the background is a linear interpolation of the OD at the endpoints of integration. The accuracy of this formula is reported to be ±10% [55].

We can also use the other ortho-induced $Q_1(0)$ absorption lines at 4737-4742 cm^{-1} to calculate the ortho fractions. The disadvantage of the $Q_1(0) + S_0(1)$ transition is that it's sitting on the broad shoulder of the $S_1(0)$+ phonon transition, and is slightly lower in amplitude (although bigger in area) as compared to $Q_1(0) + Q_0(1)$ transition. However, it is advantageous for our current optical setup because it is at a frequency where we have more light, and no significant absorption lines in the air as compared to the $Q_1(0) + Q_0(1)$ transition at 4151-4154 cm^{-1}. In this work, we choose to use the $Q_1(0) + S_0(1)$ transition to measure the orthohydrogen fraction.

We were initially unable to find a literature value for the relation between the $Q_1(0) + S_0(1)$ optical depth and the orthohydrogen fraction, so we calibrated it using the $Q_1(0)$+ $Q_0(1)$ absorption feature, as shown in figure 4.4. We performed the calibration by comparing the integrated areas of the $Q_1(0) + S_0(1)$ and $Q_1(0) + Q_0(1)$ transitions in the OD spectrum of few of our higher temperature growths.

Using this calibration, we can calculate the ortho fraction from $Q_1(0) + S_0(1)$ transition at 4737-4742 cm^{-1} as:

$$f_{\text{ortho}} = \frac{7.87 \times 10^{-2}\ \text{mm}}{t} \cdot \int_{4737\ \text{cm}^{-1}}^{4742\ \text{cm}^{-1}} \text{OD}\, d\text{n/cm}^{-1} \tag{4.4}$$

The background optical depth is subtracted from the integral as described at the end of

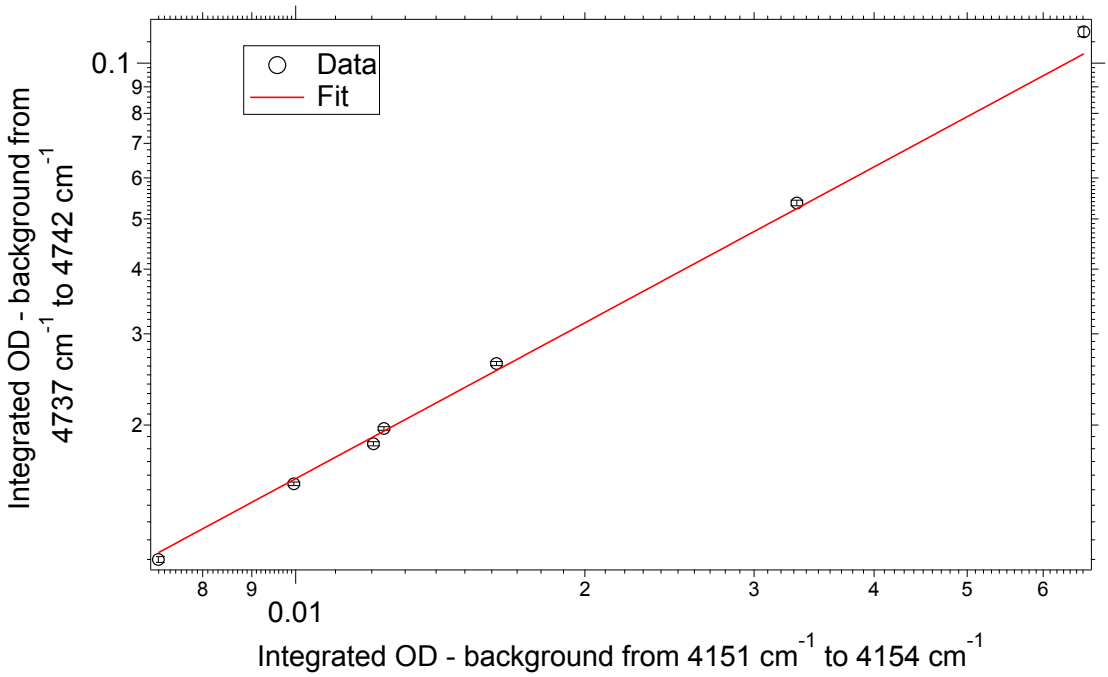

Figure 4.4: Calibration of the $Q_1(0)+S_0(1)$ line (the vertical axis) from the $Q_1(0)+Q_0(1)$ line (the horizontal axis). The data is from samples grown at temperatures from 19 K to 29 K. The background optical depth is subtracted from each integral, as described in the text. The data are fitted into a line (y=a+bx) with a=0 and b=1.58.

this section.

We found a small systematic error in formula 4.4, as the $Q_1(0)+S_0(1)$ transition was observed to broaden with increasing orthohydrogen fractions. This is explained in section 4.2.1. For OP converter temperatures between 16 and 29 K, the measured linewidth increases roughly linearly from a FWHM of 0.8 to 1.0 cm^{-1}. This leads to a variation in the "fraction" of the $Q_1(0) + S_0(1)$ transition contained within the finite region of integration of equation 4.4. We estimate that, for the orthohydrogen fraction range explored in this work, this leads to errors in f_{ortho} of $\lesssim 11\%$. At larger orthohydrogen fractions, this error would likely increase.

Also, for the fit, the rms fractional deviation of our data from the fit is 4.45%. Combining this error with the systematic error due to line broadening and the claimed accuracy of

reference [55], we estimate the accuracy of formula 4.4 to be ±15% over the range of conditions explored in this work.

During the preparation of the manuscript to publish this work, we became aware of a prior measurement of the $Q_1(0) + S_0(1)$ transition by Raston, Kettwich, and Anderson [56]. Their method of spectral analysis — which integrates over a wider wavelength range than equation 4.4 — is capable of providing accurate results at high ortho fractions. Our narrower range of integration provides lower noise for the measurement of low ortho fractions. The coefficient of equation 4.4 is consistent with the transition strength of reference [56] to within the stated errors of the two works.

For the low temperature growths, the ortho fraction is low, and consequently the $Q_1(0)$+ $S_0(1)$ absorption feature exhibits poor signal to noise. This absorption feature is located on the phonon sideband of parahydrogen transition. So we used the following to substract off the background. First, we selected our region of interest (ROI) in the OD curve (i.e., 4737-4742 cm^{-1}). On both sides of the region of interest (ROI) we integrate the optical depth of 5 adjacent regions of the same width as the ROI. The resulting 10 "background" points are fit as a function of their center wavelengths to a 4th-order polynomial. (The ROI is excluded from this fit). The difference between the area of selected range and the fit gives us the integrated OD. We then use this polynomial to calculate the background in the ROI. We estimate the statistical error of our measurement from the chi-square value for the fit, the number of fitted points (i.e. 10) and the number of fit parameters (i.e. 4). The error is determined as:

$$\text{error} = \sqrt{\frac{\chi^2}{\text{number of fitted points} - \text{number of fit parameters}}}$$

4.2.1 Linewidth broadening and Systematic erorrs

For calculating the ortho fraction of the sample, we are using $Q_1(0) + S_0(1)$ transition around 4740 cm^{-1} as discussed in section 4.2. However, we observed the line broadening of $Q_1(0) + S_0(1)$ transition for samples grown at higher OP converter temperatures. Figure 4.5 shows the variation of linewidth as a function of OP converter temperature. For OP temps between 16 and 29 K, the line width increases linearly from 0.80 to 1.02 cm^{-1}.

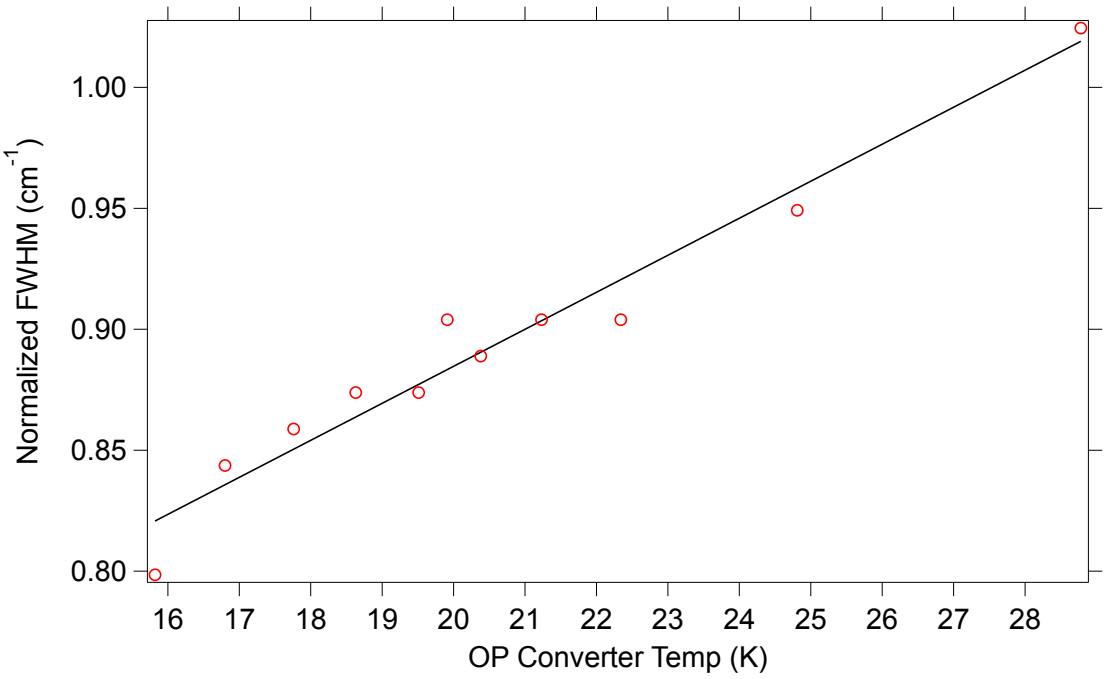

Figure 4.5: Line width of the normalized $Q_1(0) + S_0(1)$ transition as a function of OP converter temperature..

It should be noted that while calculating the area under the transition curve, we select a finite range of integration: 4737 cm^{-1} to 4742 cm^{-1}. This variation in linewidth results in the error on determining the area under the given integration range. According to equation 4.4, this error in the area introduces error in the calculated ortho fraction. To account for this, we explored the variation OD area of the normalized $Q_1(0) + S_0(1)$ transition as a function of integration range. Typically, we select 5 wavenumbers wide

integration range from 4737 cm^{-1} to 4742 cm^{-1} for our calculations. But to study the effect of linewidth issue on the integrated OD area, we calculated the area under the transition curve for different integration ranges, and plotted them. Figure 4.6 shows that the OD area of this feature within 5 wavenumbers wide calibrated range is less than the total area of this transition under a 20 wavenumber integration range. The area varied by as much as 11% for the growth at 28.95 K. The purple curve in the plot represents the normalized OD area for the growth at OP converter temperature of 19.54 K. The ortho transition for this growth has relatively lower signal as compared to the growths at higher OP converter temperature, and hence suffers from low signal to noise when normalized. This causes the normalized OD area to decrease as the integration range is increased.

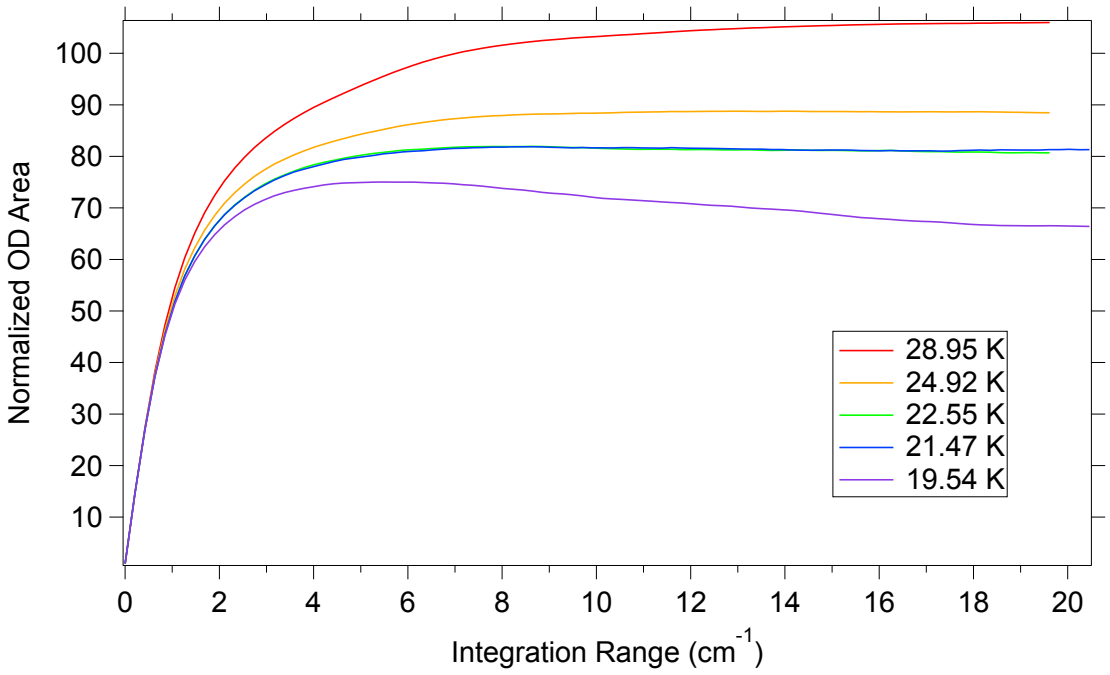

Figure 4.6: OD area of the normalized $Q_1(0)+S_0(1)$ transition as a function of integration range.

4.3 Measurement of HD fraction

To measure the HD fraction in the sample, we used the $Q_1(0)_{H_2} + S_0(0)_{HD}$ transition at 4420 cm^{-1}. While we were unable to unable to find a literature value relating the optical depth to the HD fraction f_{HD}, Crane and Gush [53] have published spectra of parahydrogen samples with known HD fractions presented in figure 4.7.

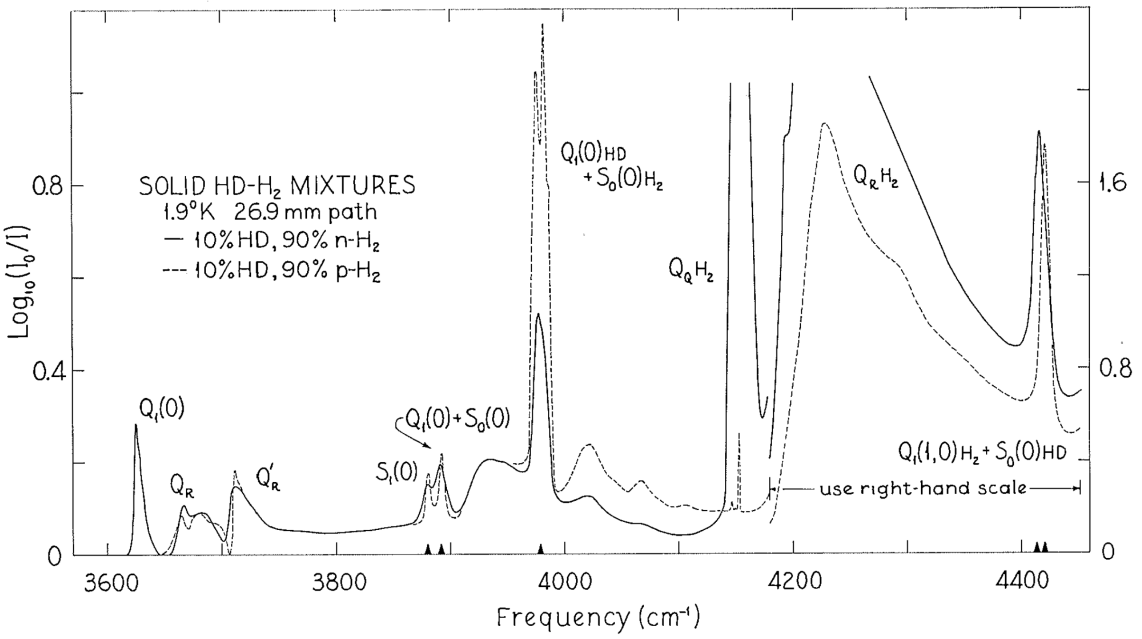

FIG. 6. The induced absorption spectrum of the solid mixture 10% HD – 90% H_2. The spectral resolution limit is 0.4 cm^{-1}.

Figure 4.7: Figure reproduced from reference [53].

Figure 4.7 includes the induced absorption spectrum of the solid mixture of 10% HD and 90% parahydrogen. Though it is a larger HD fraction as compared to the range explored in our work, we used the HD transition around 4420 cm^{-1} to establish the relation between HD fraction and the integrated OD of the transition peak. From their spectra, we find in the low HD limit,

$$f_{HD} = \frac{8.96 \times 10^{-2}\ \text{mm}}{t} \int_{4416\ \text{cm}^{-1}}^{4424\ \text{cm}^{-1}} \text{OD}\, d\text{n/cm}^{-1} \tag{4.5}$$

with an estimated accuracy of ±10%.

The $Q_1(0)_{H_2} + S_0(0)_{HD}$ transition used to measure the HD fractions is located on the phonon sideband of parahydrogen transitions. At low HD fractions, this background optical depth is much larger than that of the transition of interest. To subtract the background, we followed the same procedure as explained in section 4.2.

Chapter 5

Results

5.1 Sample growth rate

For a hydrogen flow rate of 4 sccm, the measured sample growth rates ranged from 0.10 mm/hr to 0.25 mm/hr for all of our growths. We were able to carry out the successful growth of parahydrogen samples at OP converter temperature as low as 8.1 K. The sample growth rate during the end of the growth at 8.1 K was 0.19 mm/hour.

However, attempts to grow at OP converter temperature < 8 K were unsuccessful. An attempt to grow at an OP temperature of 7.62 K resulted in a low deposition rate of ~ 0.07 mm/hr for roughly 158 minutes, before the flow stopped. This was verified by the drop in MFC signal and the FTIR spectrum. We interpret this as clogging the OP converters with hydrogen.

The sample growth rate is the interplay between the sample sublimation rate, the flux of incoming H_2 molecules at the sapphire window and their sticking probability. We present their effects in the following discussion.

Estimate of sample sublimation rate

Velocity of a gas molecule is related to its temprerature as given by [57]:

$$KE_{avg} = \frac{1}{2}Mv_{avg}^2 = \frac{3}{2}N_A k_B T \implies v_{avg} = \sqrt{\frac{3N_A k_B T}{M}} \tag{5.1}$$

where, $N_A = 6.023 \times 10^{23}$ is Avogadro's number, M is the molar mass and k_B is the Boltzmann constant.

From ideal gas law $PV = Nk_BT$, we estimate the density of gas-phase atoms around the solid sample:

$$n = \frac{N}{V} = \frac{P}{k_B T} \tag{5.2}$$

Then, the flux can be calculated as:

$$\text{Flux} = \text{Density} \times \text{Velocity} = \frac{P}{k_B T} \times \sqrt{\frac{3N_A k_B T}{M}} = \sqrt{\frac{3N_A P^2}{k_B T M}} \tag{5.3}$$

Here, P is the vapor pressure of H_2 molecules at a given temperature T.

Consider the case of a thin sample where sublimation only matters on the large face. The sample is deposited on the sapphire window. So, the sublimation is only possible from one exposed face i.e. the face where we are depositing parahydrogen gas. In that case,

Change in number of molecules = Flux × Area

$$\text{Change in volume of the sample} = \frac{\text{Flux} \times \text{Area}}{\rho_N}$$

$$\text{Change in thickness of the sample} = \frac{\text{Flux} \times \text{Area}}{\rho_N \times \text{Area}} = \frac{\text{Flux}}{\rho_N}$$

Here ρ_N is the number density of the solid H_2 which has a value 2.6×10^{28} m^{-3} [12].

Hence, the change in thickness due to sublimation can be calculated by dividing the flux by the number density of the solid H_2. Equation 5.3 shows a dependence of flux with the vapor pressure. The natural logarithm of vapor pressure for molecular H_2 as a function of temperature is reported in literature [58] as:

$$\ln(P) = 7.570953 - \frac{86.94152}{T} + 2.860678\ln(T) \tag{5.4}$$

Substituting this for P in equation 5.3, we can calculate change in sample thickness due to sublimation as:

$$\text{Change in sample thickness} = \frac{N_A}{\rho_N \sqrt{R \cdot T \cdot M}} \exp\left(7.570953 - \frac{86.94152}{T} + 2.860678\ln(T)\right) \tag{5.5}$$

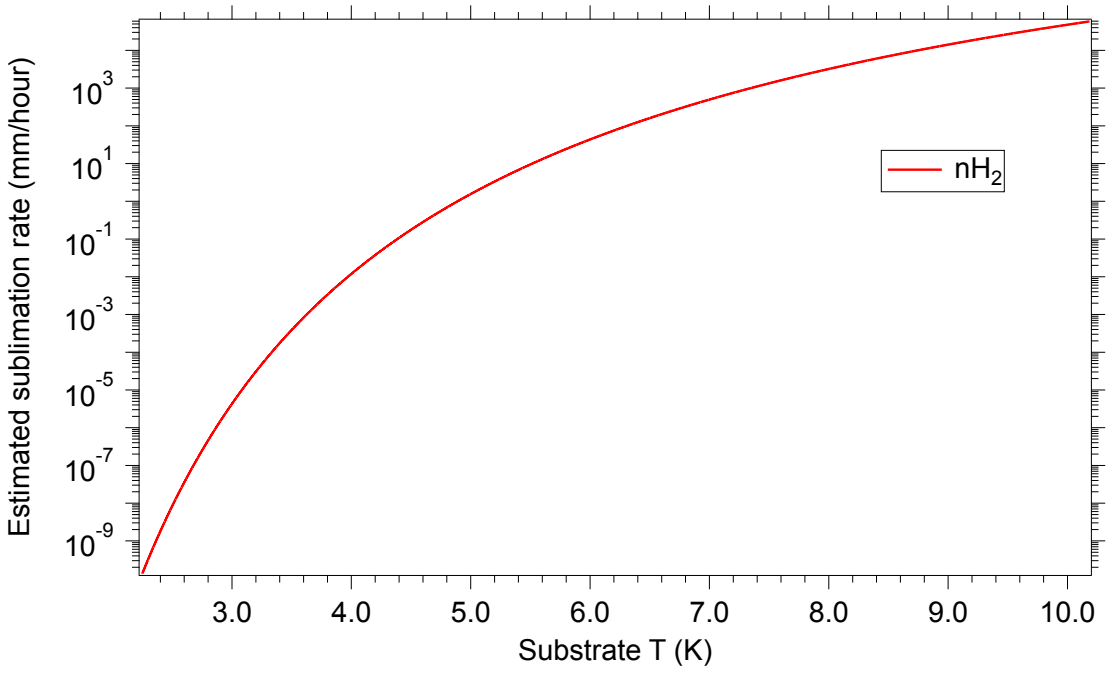

Figure 5.1: The estimated sample sublimation rate for molecular H_2 plotted as a function of the substrate temperature.

Our calculation shows that the sample sublimation rate depends on the substrate temperature; higher substrate temperatures result in higher sublimation rate. Our calculation shows that for the growths at OP converter temperature 14 K and 20.5 K (the substrate temperatures are 4.5 K and 4.6 K respectively), the sublimation rate is significant and is responsible for limiting their growth rates. However, the sublimation for the growths with substrate temperature $\leq$ 4.4 K seems to have negligible effect on the sample growth rate. This can be seen in the data presented in figure 5.2.

Flux of incoming H_2 molecules

We maintained consistency in the flow rate of 4 sccm during our growths. However, that does not necessarily imply that the flux of incoming H_2 molecules on the sapphire window is constant. The collimation of the incident beam of H_2 molecules onto the substrate dictates the flux of incoming H_2 molecules. At higher OP converter temperatures, the molecules have higher kinetic energy. This could result in spreading of the gas molecules between the hydrogen output and the substrate and hence could limit the number of molecules reaching the substrate.

Sticking probability

The sticking probability for H_2 on different surfaces depends on the temperature of incoming gas beam. It has been reported in the literature that the sticking probability of hydrogen molecules (on various surfaces) falls significantly as the temperature of the incident beam increases [59, 60].

Figure 5.2 shows the measured growth rate for different samples, plotted as a function of the average OP converter temperature during sample growth. The growth rate of the sample shows a significant dependence on both the temperature of the second-stage OP converter and, at sufficiently high substrate temperatures, the substrate temperature as

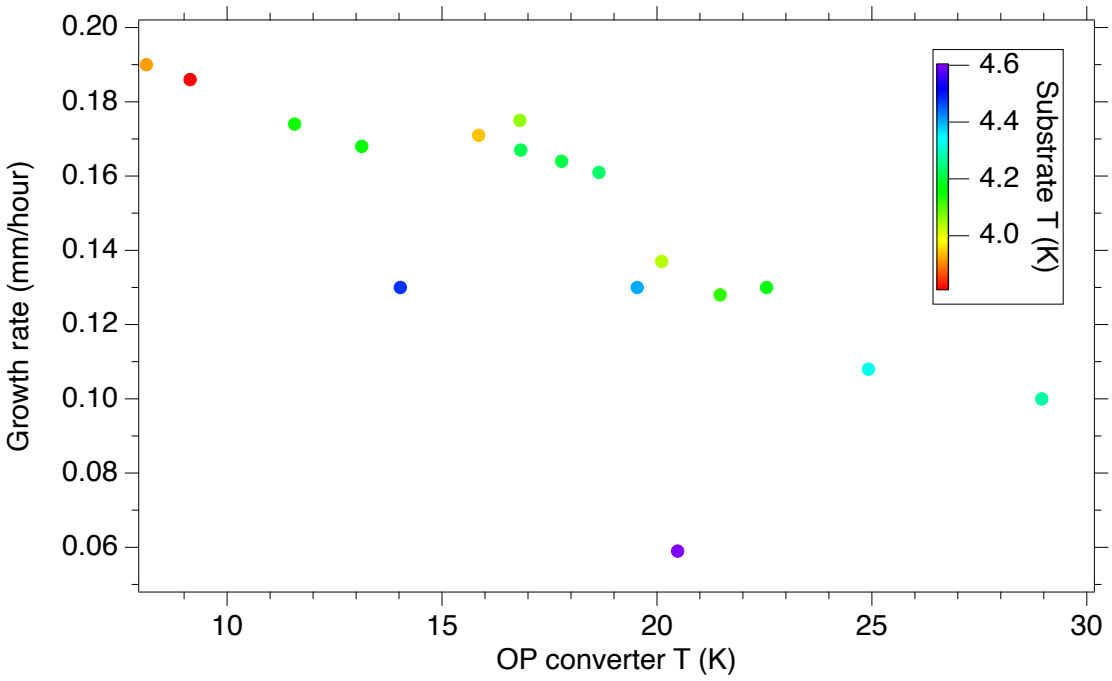

Figure 5.2: The measured growth rate of different samples, plotted as a function of the average OP converter temperature during sample growth. The data points are colored according to the average substrate temperature during growth.

well. The two sample growths at substrate temperatures $\gtrsim$ 4.4 K suffer from high sample sublimation rate (as compared to the deposition rate) based on the calculations mentioned before. However for all growths at substrate temperature <= 4.4 K, where sample sublimation is not an issue, appears to have a linear dependence on the OP converter temperature. Although we do not understand the reason completely, we assume that it is governed by the collimation of the H_2 gas beam towards the substrate and the sticking probability of the atoms to the substrate. With the higher OP converter temperature, the incoming gas beam has higher beam temperature and consequently would be expected to have a lower sticking probability resulting to the slower growth rates. We speculate that the decrease in the growth rate with increasing OP converter temperature is primarily due to a change in the sticking probability of hydrogen molecules.

5.2 Ortho fraction

The results of our measurements of the orthohydrogen fraction of 20 separate samples for a flow rate of 4 sccm are shown in figure 5.3.

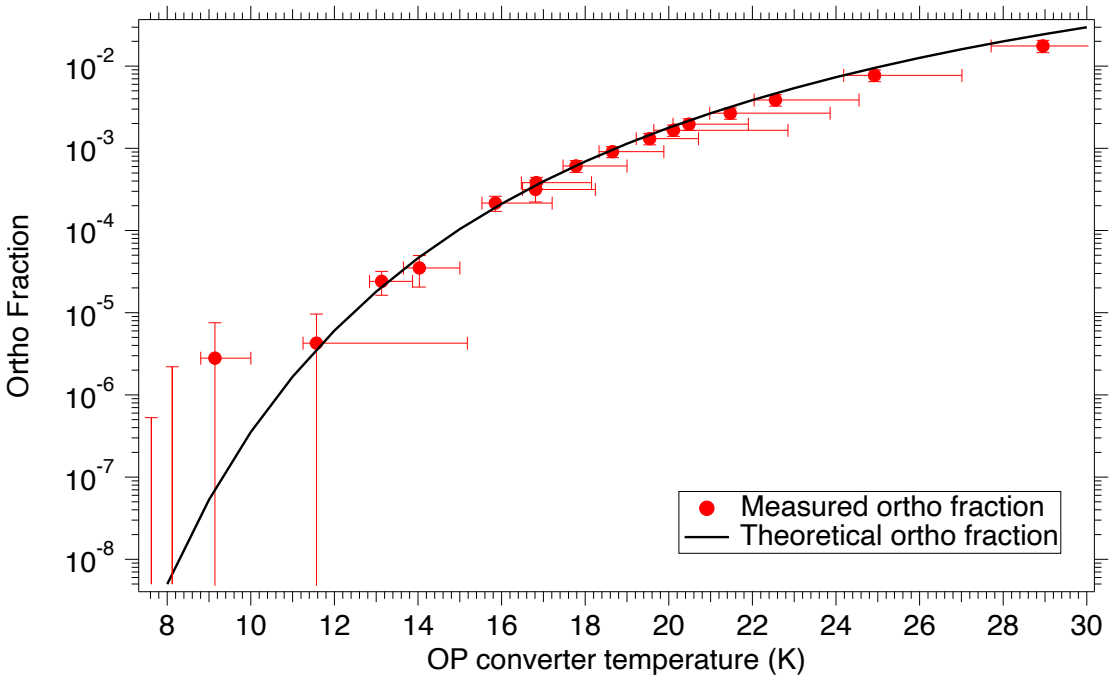

Figure 5.3: Measurements of the orthohydrogen fraction in deposited samples, plotted as a function of the OP converter temperature during sample growth. The temperature shown is the average temperature of the OP converter during deposition; the temperature error bars indicate the range of temperatures during growth. Not included in the temperature error bar is the ±0.2 K accuracy of the thermometer. The orthohydrogen fraction error bar represents the statistical error of the meaurement; not included is the ±15% uncertainty due to the accuracy of our spectroscopy calibration. For comparison, the expected orthohydrogen fraction in thermal equilibrium is shown a function of temperature [12].

The experimental spectroscopic results obtained for the ortho fraction shows the expected behavior. The measured orthohydrogen fractions are consistent– within our experimental error– with reaching thermal equilibrium at the given OP converter temperature.

Due to better signal-to-noise of our spectroscopic measurements for the higher temper-

ature growths, we can measure the orthohydrogen fraction in the high OP converter temperature regime. However, at our coldest temperatures, the signal-to-noise of our spectroscopic measurements is less than one, and we can only put an upper limit on the ortho fraction. A weighted average of the ortho fractions for the growths with OP converter temperature $T < 10$ K gives an upper limit on the ortho fraction of 1×10^{-6} at 95% confidence. To confirm whether our OP converter is still achieving the expected "equilibrium" ortho fractions at temperatures $\lesssim 11$ K will require a more sensitive probe of the ortho fraction than is achievable with our current spectroscopy. If the OP converter is functioning equally well at our coldest temperatures as it was at higher temperatures, the ortho fraction should be in the order of 10^{-8}.

5.3 HD fraction

Hydrogen atom exists in various isotopic forms. The naturally occuring isotopes of hydrogen are protium (A=1) and deuterium (A=2). The nucleus of protium consists of a single proton whereas the deuterium nucleus consists of a proton and a neutron. Protium and deuterium have natural abundance of 0.99985 and 1.5×10^{-4} respectively [61]. A hydrogen (H_2) molecule is made up of two protium atoms and a deuterium (D_2) molecule is made of two deuterium atoms. However, if a protium atom combines with deuterium atom, it forms hydrogen deuteride (HD) molecule. Assumuing that the bond strength between the constituent atoms of H_2, D_2 and HD molecules are similar, a fraction of 3×10^{-4} would be expected for HD from the natural abundance of deuterium [61].

We measured the HD fraction f_{HD} spectroscopically as described in section 4.3. We found that our OP converter, if operated at sufficiently low temperatures, also provides isotopic purification of the hydrogen gas. This is advantageous for creating a non-

magnetic matrix. As the ground state of the HD molecule has a nonzero nuclear spin, it has a magnetic moment associated with its nuclear spin. This magnetic moment could possibly play a role to limit the T_2 and T_2^* of implanted spin qubits.

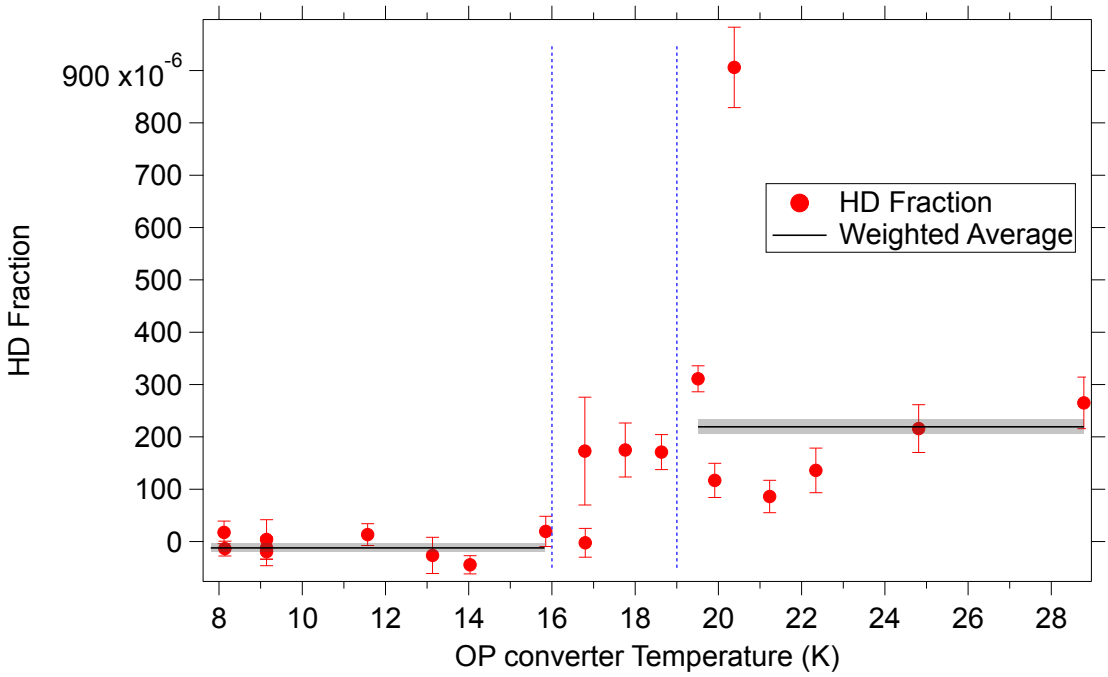

Figure 5.4: Measurements of the HD fraction in deposited samples, plotted as a function of the OP converter temperature during sample growth. The temperature shown is the average temperature of the OP converter during deposition. The orthohydrogen fraction error bar represents the statistical error of the meaurement; not included is the ±10% uncertainty due to the accuracy of our spectroscopy calibration.

The results of our measurements of the HD fraction of 20 separate samples are shown in figure 5.4. For the OP converter temperatures > 19 K, the measured HD fraction is inconsistent from sample to sample. The weighted average of measurements from 7 separate samples above 19 K give an HD fraction of $2.2 \times 10^{-4} \pm 0.15 \times 10^{-5}$ with the Chi-Squared value of 126.5. The standard deviation of 7 points from the fit is $\pm$ 2.8×10^{-4}.

For the OP converter temperatures < 16 K, the HD fraction is too small to measure, and the weighted average of measurements from 10 separate samples below 16 K give

an HD fraction of $-1.1 \times 10^{-5} \pm 0.7 \times 10^{-5}$ with the Chi-Squared value of 8.5. The standard deviation of 10 points from the fit is $\pm 2.1 \times 10^{-5}$.

While we did not originally anticipate this isotopic purification of the hydrogen gas, in retrospect it is not a surprising result. We speculate the effect is due to the slight differences in the vapor pressure of the different isotopes of hydrogen, as seen in figure 5.5. These slight differences are likely "amplified" by flowing the gas through a tube filled with ortho-para catalyst: flowing hydrogen gas over a granular media at cryogenic temperatures is a demonstrated method for isotopic purification [62, 63]. We note that prior parahydrogen research noted that HD and D_2 condense at higher temperatures than H_2, and that this effect can eventually cause clogging of the OP converter [64].

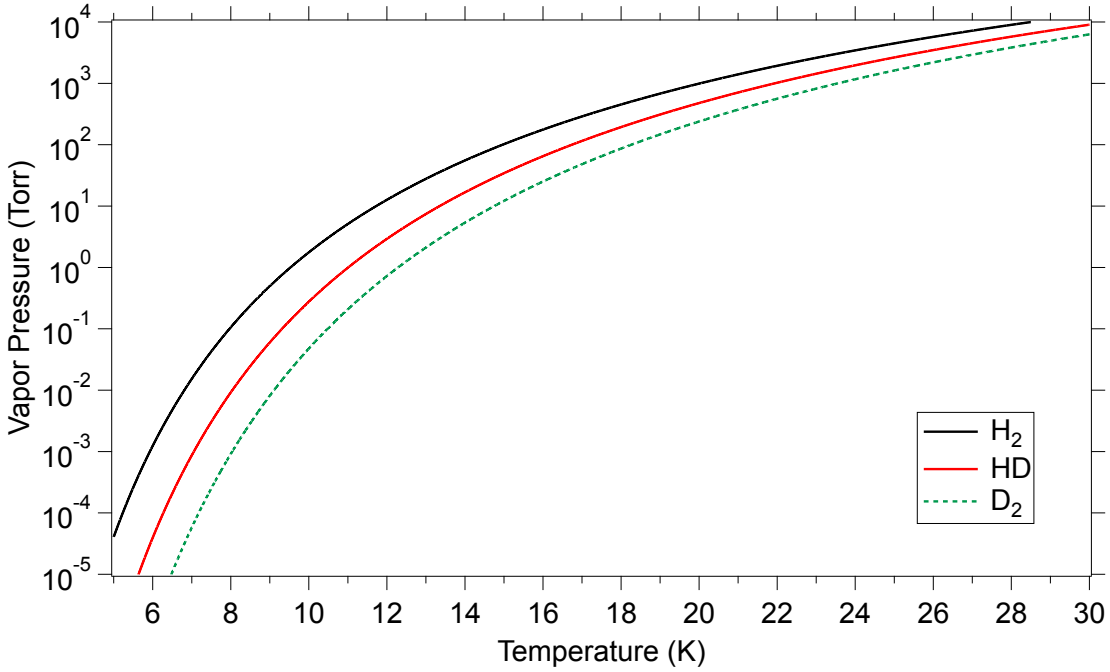

Figure 5.5: The equilibrium vapor pressures of H_2, HD, and D_2, from reference [58].

Chapter 6

Sample Growth at Higher Flow Rates

In this chapter, we tried to investigate the sample growth with higher flow rates. The maximum flow rate at which our mass flow controller (MFC) can operate is 21 sccm. After an unsuccessful growth at 21 sccm, we performed a successful sample growth at the flow rate of 17 sccm with a growth rate of 0.7 mm/hour– the highest sample growth rate achieved with our apparatus. Other research groups have performed similar vapor deposition experiments and have grown parahydrogen samples at rates up to 5 mm/hour [65]. However, they used two cryocoolers in their experiment to cool the OP converter and the cold finger separately. If the thermal link between the coldfinger and the second stage cryocooler head is improved, we speculate that our design with a single cryocooler would be capable of growing samples at higher hydrogen flow rates than achieved in this work.

6.1 Failed growth at flow rate of 21 sccm

In an attempt to explore sample growth at higher flow rate, we started with the highest flow rate our MFC could operate i.e. 21 sccm. However, the attempt was unsuccessful,

and we attribute this to a process of “thermal runaway”. During thermal runaway, the temperature of coldfinger rises due to the thermal load of incoming gas beam, which in turn limits the ability of substrate to condense gas beam (as explained in section 5.1). Then the pressure inside the cryostat increases which again increases the temperature of coldfinger. Due to this, we do not observe sample growth.

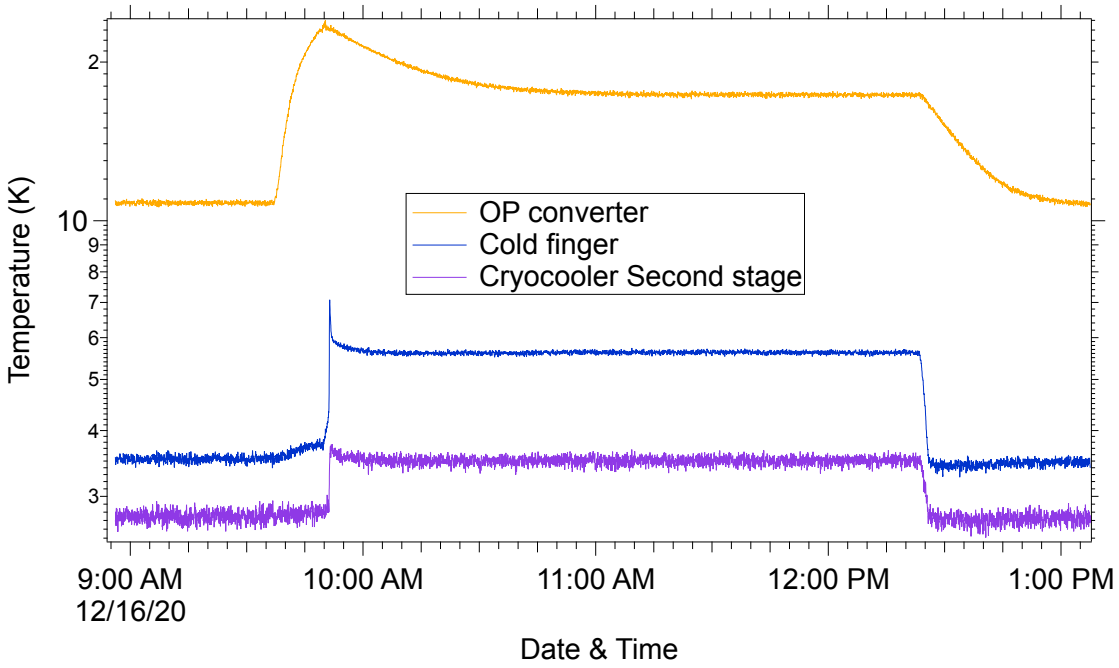

Figure 6.1: The temperature curve for various parts of cryostat during the sample growth attempt at 21 sccm plotted against the date and time of measurements.

Figure 6.1 shows the temperature of OP converter, coldfinger and cryocooler second stage during the thermal runaway at 21 sccm flow rate. At 9:35 AM and 12:23 AM, the MFC was turned on and off respectively. Starting from its base temperature of 11 K, the temperature of the OP converter begins to rise as we turn on the gas flow. The temperature rises due to large thermal load caused by adsorption of hydrogen on the surface of the catalyst. Once the gas starts exiting the OP converter, the temperature of OP converter decreases while the temperature of cold finger and cryocooler second stage increases. But due to the thermal load, thermal runaway occurs and the temperatures

of the cold finger and cryocooler second stage rises quickly.

As we keep pumping on the cryostat during the sample growth, the temperature and pressure inside the cryostat reaches the steady state. During the steady state, the temperature of coldfinger and that of cryocooler second stage were 5.6 K and 3.5 K respectively.

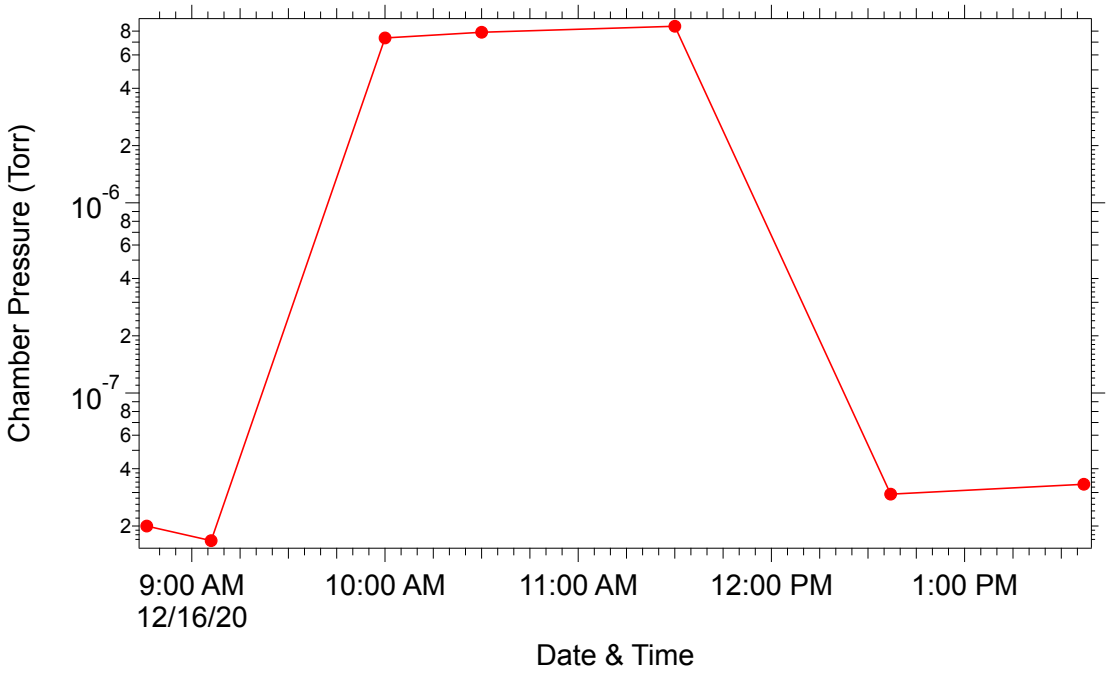

Figure 6.2: Total chamber pressure measured by RGA plotted against date and time of measurement.

Figure 6.2 is a plot of chamber pressure measured by RGA during the experiment performed using 21 sccm flow rate. The flat curve during thermal runaway represents the steady state where there was no sample growth. The chamber pressure during the thermal runaway is greater than the pressure during the successful sample growth at 17 sccm by an order of magnitude.

6.2 Growth at flow rate of 17 sccm

We were able to carry out a successful sample growth at a flow rate of 17 sccm. During this sample growth, the OP converter was held at a temperature of 14.8 K, while the cold finger was 3.7 K during the deposition. After 8 minutes of delay in deposition, the sample growth started. By the end of this growth, the overall sample growth rate was 0.7 mm/hour.

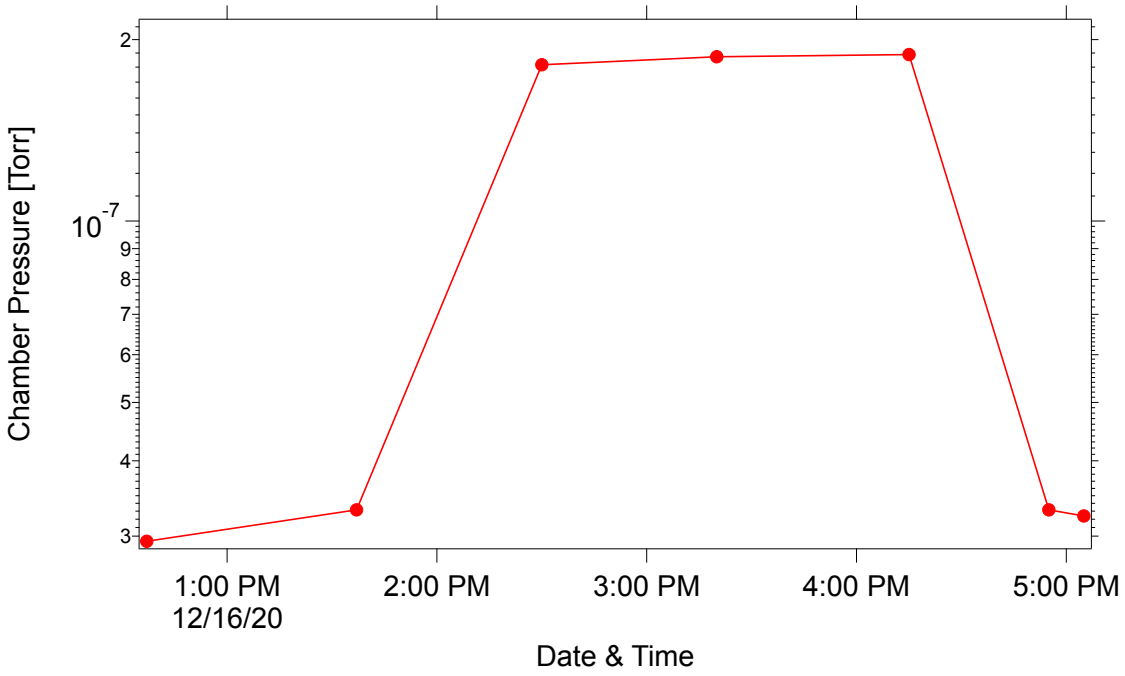

Figure 6.3: Total chamber pressure measured by RGA plotted against date and time of measurement.

Figure 6.3 is a plot of chamber pressure measured by RGA during the sample growth at 17 sccm flow rate. The data between timestamps 1:35 PM and 4:23 PM represents the chamber pressure during a successful sample growth at 17 sccm.

Ortho Fraction

The OP converter temperature during this sample growth is 14.8 K which corresponds to the equilibrium ortho fraction of 9×10^{-5}. However, our spectroscopic measurement

of ortho fraction for this sample is $1.2 \times 10^{-4} \pm 4.16 \times 10^{-6}$. The measured ortho fraction is higher by a factor of 1.3 compared to the expected ortho fraction, and this is equivalent to the increase in temperature of 0.4 K for the OP converter. We speculate that at higher flow rates, the interaction time of hydrogen molecules with the catalyst is reduced so that the thermal equilibrium is not attained. And hence we are left with higher fraction of orthohydrogen in our sample. We also speculate that the difference might have occurred due to heating of the catalyst by the gas flow. Since our temperature sensor is placed on the copper block holding the OP tubing instead on the OP tubing itself, our thermometry does not measure the temperature of the catalyst directly.

HD fraction

The measurements on the HD fraction for this sample gave $2.02 \times 10^{-4} \pm 1.94 \times 10^{-5}$ which is slightly less than the natural abundance of HD[61].

Chapter 7

Conclusions

The objective of the experiment presented in this thesis was to grow a highly pure parahydrogen sample. The previous experiments performed to grow high-purity parahydrogen samples are discussed in section 1.3. Some prior work implied it was impractical to extract hydrogen if the catalyst temperature is much below the triple point of hydrogen at 13.8 K [66, 55], which would limit the orthohydrogen fraction to levels $\gtrsim 10^{-5}$. In the prior literature, catalyst temperatures down to $\sim$ 13 K were reported, and orthohydrogen fractions $\lesssim 10^{-4}$ were verified spectroscopically [24, 67, 27, 29].

We have carried out the OP conversion and sample growth within a single cryostat. With our current setup, we have successfully demonstrated the OP conversion at temperatures both above and below the liquid-solid phase transition of hydrogen and extracted the hydrogen from the catalyst as a gas. We have shown that we can operate at temperatures as low as 8 K — a temperature at which the equilibrium orthohydrogen fraction is over three orders of magnitude lower than the triple point— and spectroscopically verified orthohydrogen fractions $< 10^{-6}$.

Thus grown high-purity parahydrogen can serve as a host matrix for “matrix isolation"

experiments. In this new higher-purity regime, we now can investigate the effects of ortho fraction on the spin coherence times of the species implanted in the high-purity solid parahydrogen matrix. Also since the orthohydrogen molecules are the source of magnetic noise, a highly pure solid parahydrogen is an ideal host matrix to perform nuclear magnetic resonance (NMR) measurements in matrix isolated atoms and molecules.

Appendix A

Machine drawings

In this appendix, we present the machine drawings of various parts of our cryostat.

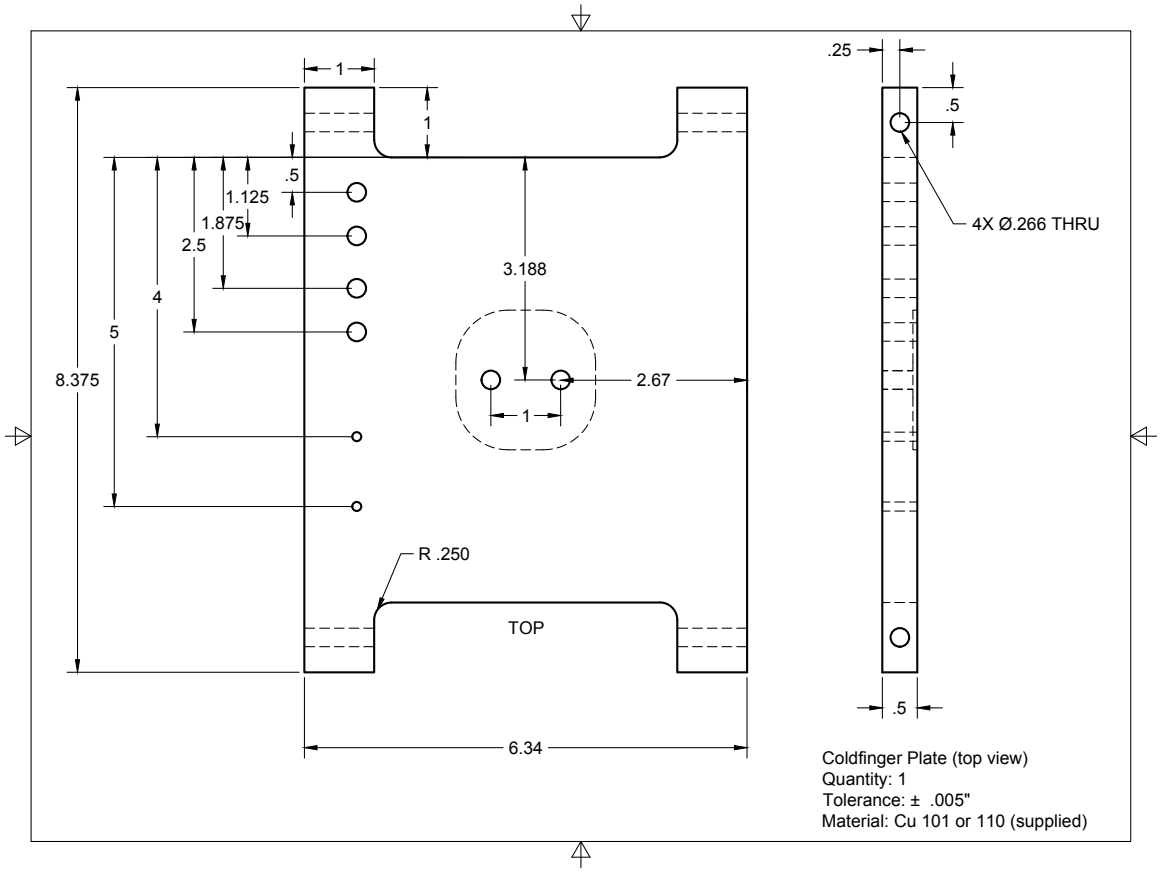

Figure A.1: Machine drawing of coldfinger plate (top view).

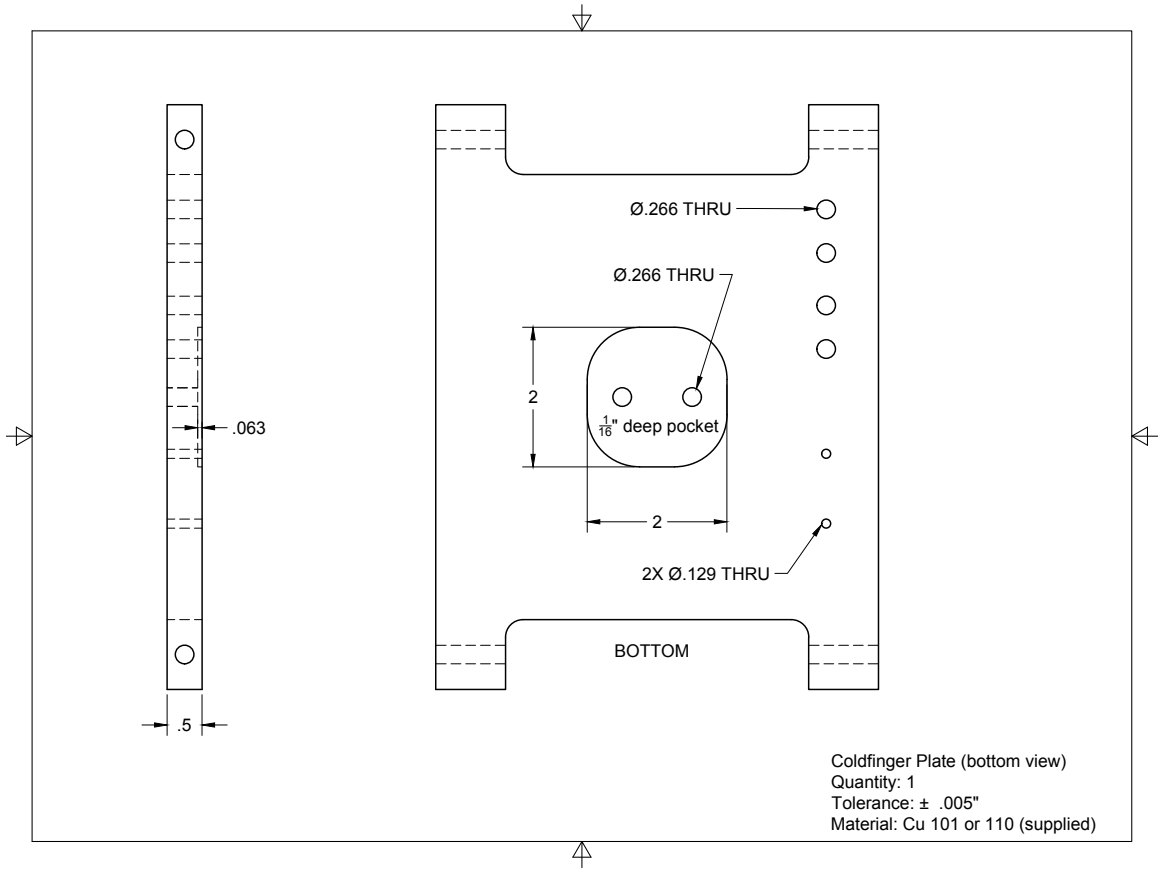

Figure A.2: Machine drawing of coldfinger plate (bottom view).

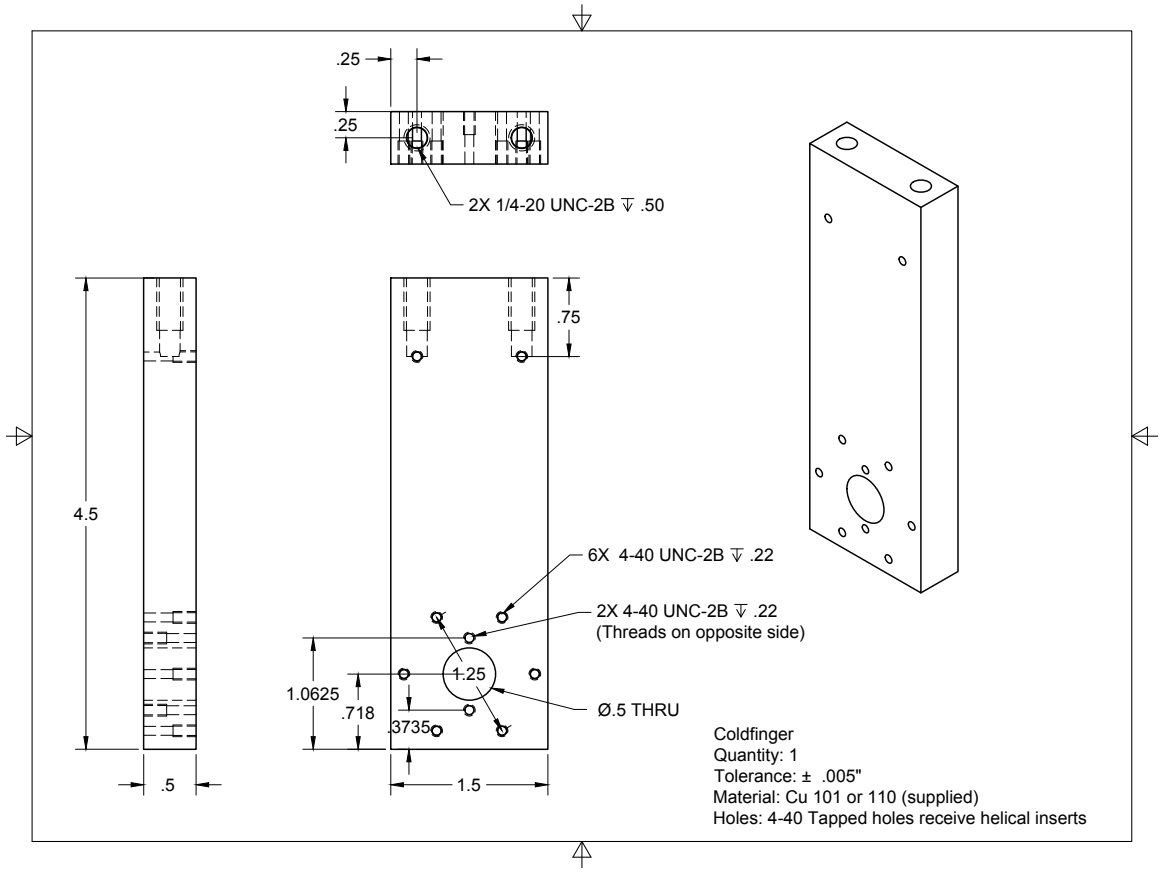

Figure A.3: Machine drawing of cold finger.

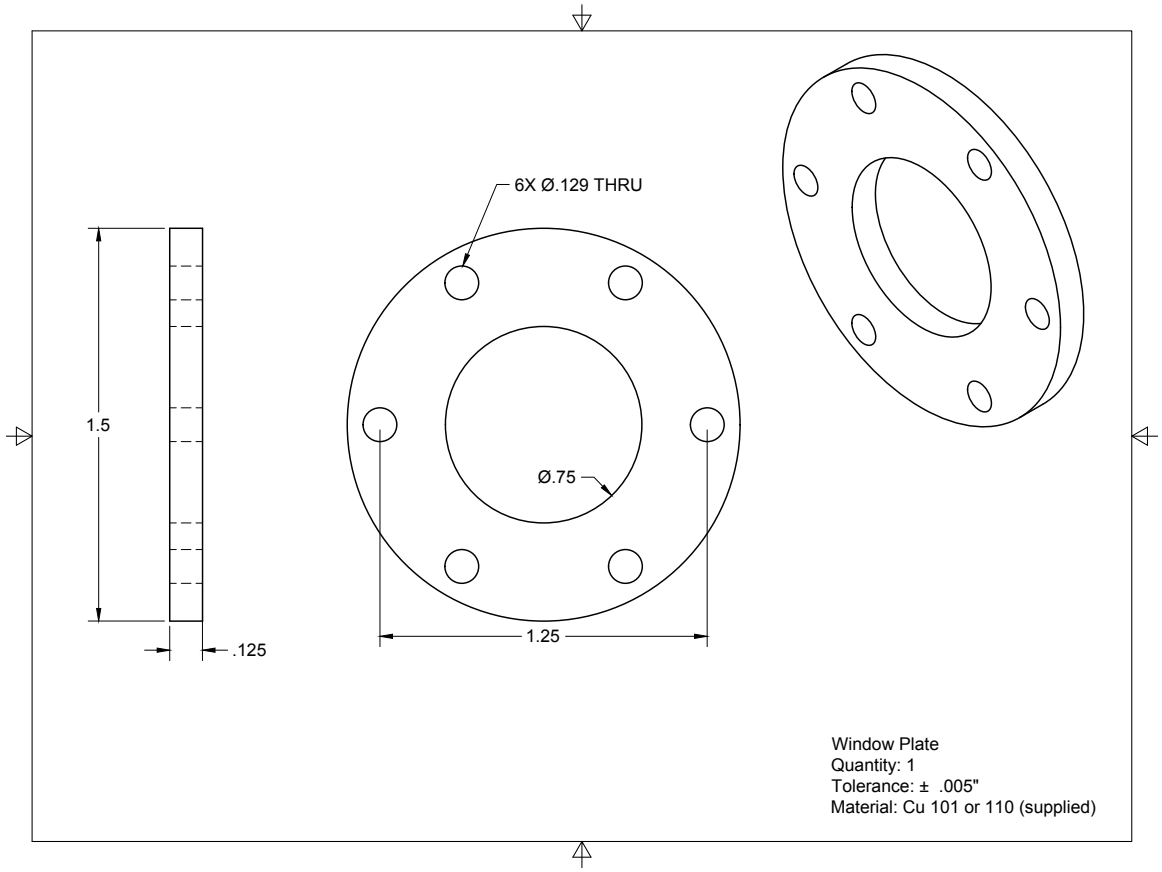

Figure A.4: Machine drawing of window plate.

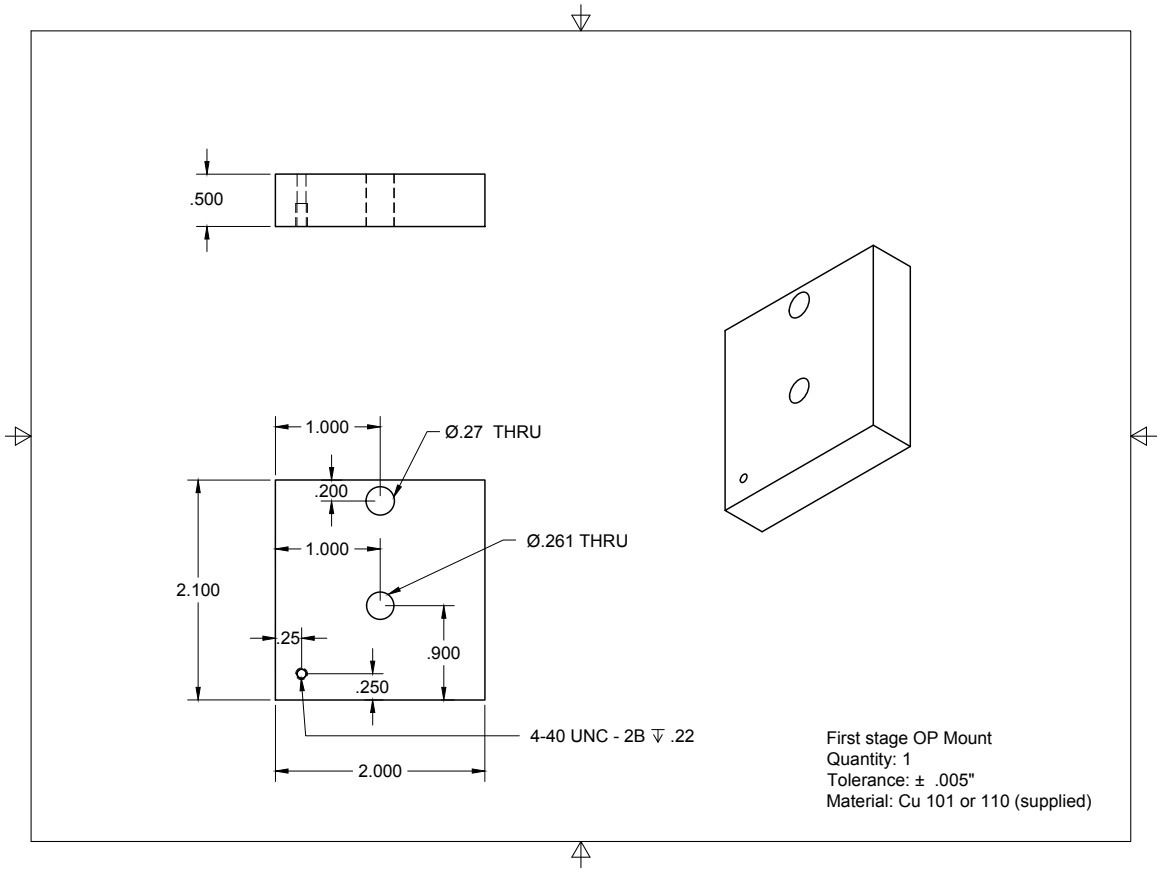

Figure A.5: Machine drawing of first stage OP mount.

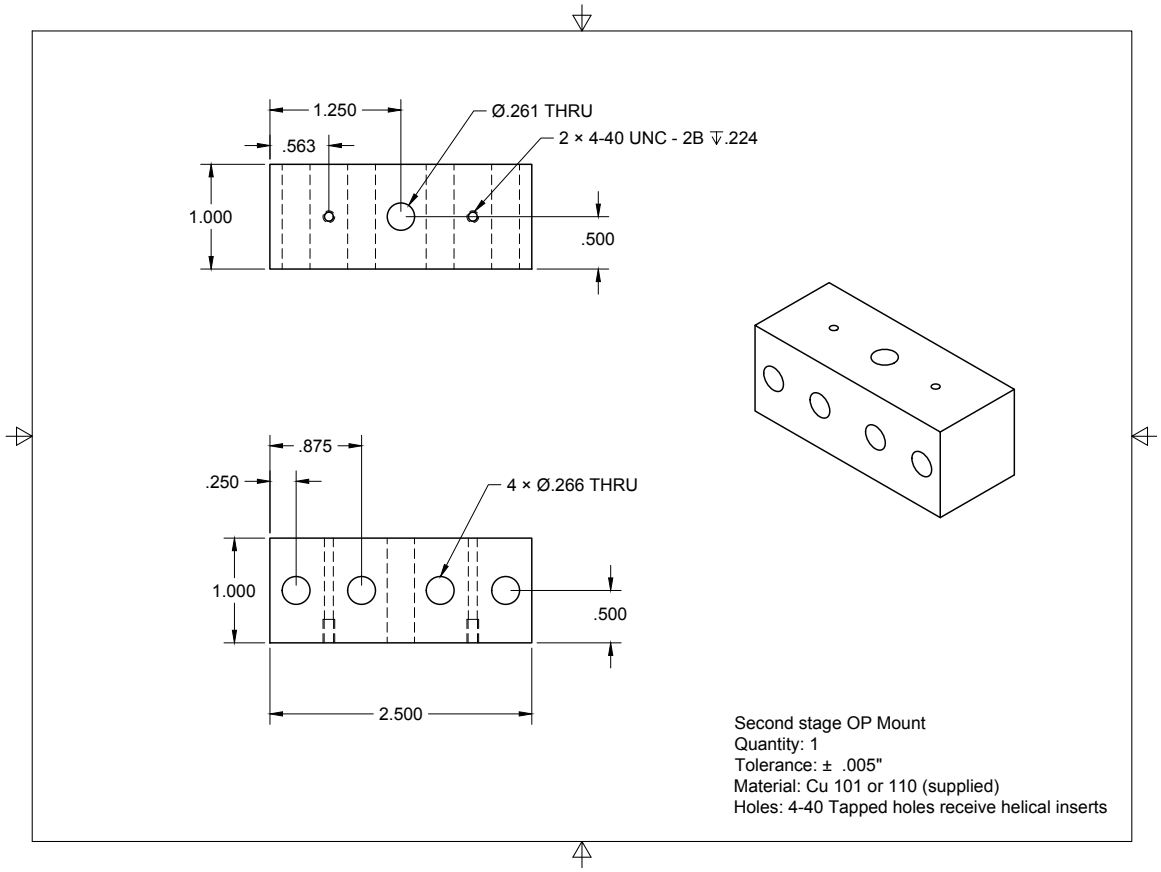

Figure A.6: Machine drawing of second stage OP mount.

Appendix B

Block diagrams for LabVIEW program

In this appendix, we present the block diagrams for the LabVIEW programs used for the data acquisition and the analog voltage output.

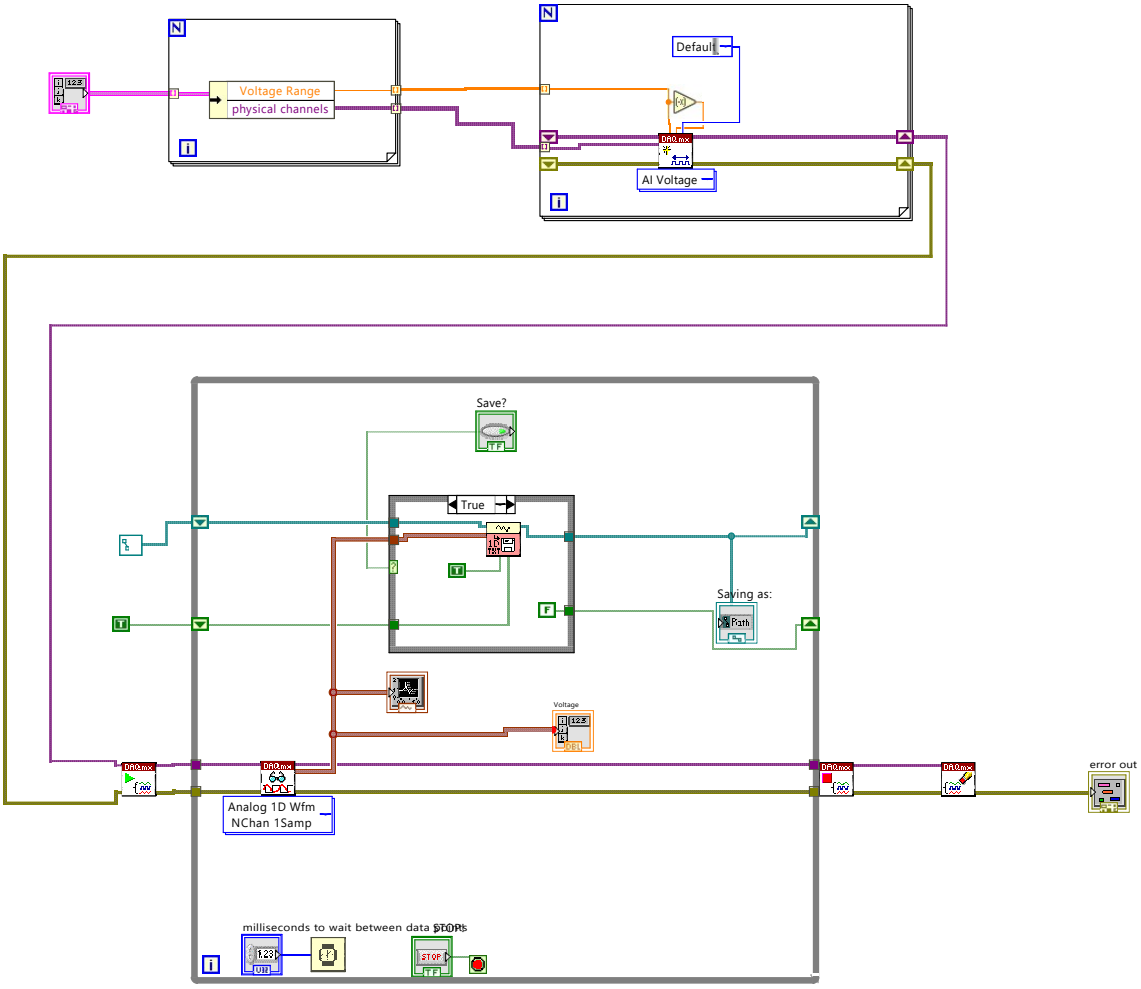

Figure B.1: Block diagram for LabVIEW program used for data acquisition.

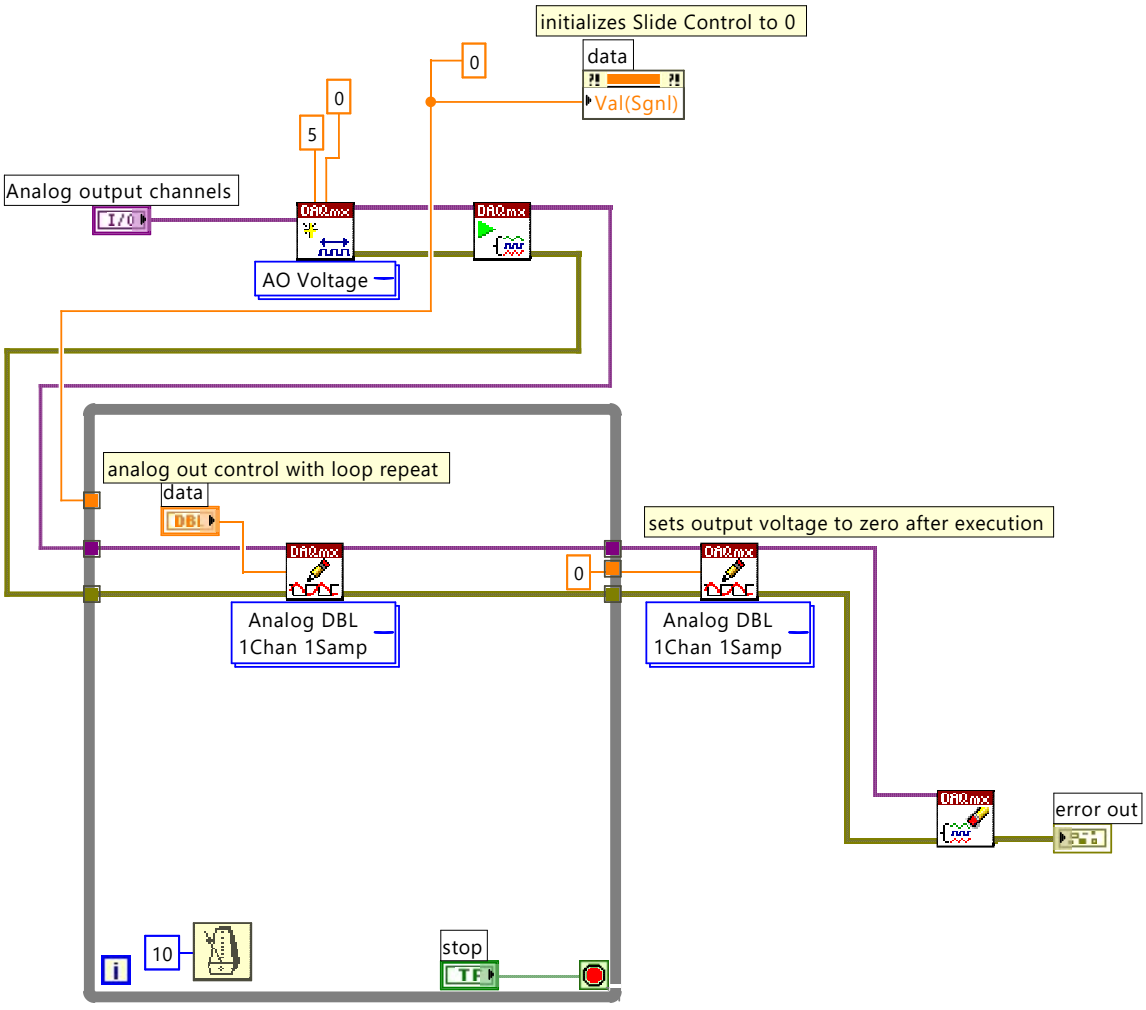

Figure B.2: Block diagram for LabVIEW program used for analog voltage output.

Bibliography

[1] Sunil Upadhyay, Andrew N Kanagin, Chase Hartzell, Tim Christy, W Patrick Arnott, Takamasa Momose, David Patterson, and Jonathan D Weinstein. Longitudinal spin relaxation of optically pumped rubidium atoms in solid parahydrogen. *Physical Review Letters*, 117(17):175301, 2016.

[2] Andrew N Kanagin, Sameer K Regmi, Pawan Pathak, and Jonathan D Weinstein. Optical pumping of rubidium atoms frozen in solid argon. *Physical Review A*, 88(6):063404, 2013.

[3] David M Lancaster, Ugne Dargyte, Sunil Upadhyay, and Jonathan D Weinstein. Radiative properties of rubidium atoms trapped in solid neon and parahydrogen. *Physical Review A*, 103(5):052614, 2021.

[4] Takamasa Momose and Tadamasa Shida. Matrix-isolation spectroscopy using solid parahydrogen as the matrix: Application to high-resolution spectroscopy, photochemistry, and cryochemistry. *Bulletin of the Chemical Society of Japan*, 71(1):1–15, 1998.

[5] Sunil Upadhyay, Ugne Dargyte, Vsevolod D. Dergachev, Robert P. Prater, Sergey A. Varganov, Timur V. Tscherbul, David Patterson, and Jonathan D. Weinstein. Spin coherence and optical properties of alkali-metal atoms in solid parahydrogen. *Phys. Rev. A*, 100:063419, Dec 2019.

[6] Sunil Upadhyay, Ugne Dargyte, Robert P. Prater, Vsevolod D. Dergachev, Sergey A. Varganov, Timur V. Tscherbul, David Patterson, and Jonathan D. Weinstein. Enhanced spin coherence of rubidium atoms in solid parahydrogen. *Phys. Rev. B*, 100:024106, Jul 2019.

[7] Sunil Upadhyay, Ugne Dargyte, David Patterson, and Jonathan D. Weinstein. Ultralong spin-coherence times for rubidium atoms in solid parahydrogen via dynamical decoupling. *Phys. Rev. Lett.*, 125:043601, Jul 2020.

[8] Victor M Acosta, Erik Bauch, Micah P Ledbetter, Charles Santori, K-MC Fu, Paul E Barclay, Raymond G Beausoleil, Héloïse Linget, Jean Francois Roch, Francois Treussart, et al. Diamonds with a high density of nitrogen-vacancy centers for magnetometry applications. *Physical Review B*, 80(11):115202, 2009.

[9] Peter Christian Maurer, Georg Kucsko, Christian Latta, Liang Jiang, Norman Ying Yao, Steven D Bennett, Fernando Pastawski, David Hunger, Nicholas Chisholm, Matthew Markham, et al. Room-temperature quantum bit memory exceeding one second. *Science*, 336(6086):1283–1286, 2012.

[10] Thaddeus D Ladd, Fedor Jelezko, Raymond Laflamme, Yasunobu Nakamura, Christopher Monroe, and Jeremy Lloyd O'Brien. Quantum computers. *nature*, 464(7285):45–53, 2010.

[11] MG Kozlov and Andrei Derevianko. Proposal for a sensitive search for the electric dipole moment of the electron with matrix-isolated radicals. *Physical review letters*, 97(6):063001, 2006.

[12] Isaac F. Silvera. The solid molecular hydrogens in the condensed phase: Fundamentals and static properties. *Rev. Mod. Phys.*, 52:393–452, Apr 1980.

[13] S Washburn, R Schweizer, and H Meyer. Nmr studies on single crystals of h 2: Iv. the hd impurity spectrum. *Journal of Low Temperature Physics*, 45(1-2):167–188, 1981.

[14] JM Delrieu and NS Sullivan. Quantum tunneling and motional narrowing of hd nmr line shapes in solid hcp h 2. *Physical Review B*, 23(7):3197, 1981.

[15] Isaac F Silvera. The solid molecular hydrogens in the condensed phase: Fundamentals and static properties. *Reviews of Modern Physics*, 52(2):393, 1980.

[16] F Schmidt. Diffusion and ortho-para conversion in solid hydrogen. *Physical Review B*, 10(10):4480, 1974.

[17] V Shevtsov, E Ylinen, P Malmi, and M Punkkinen. Quantum diffusion and catalyzed conversion of ortho-h 2 molecules in solid hydrogen. *Physical Review B*, 62(18):12386, 2000.

[18] Sunil Upadhyay. *Spin coherence and optical properties of alkali-metal atoms in solid parahydrogen*. Phd thesis, University of Nevada, Reno, 2020.

[19] K Fukutani and T Sugimoto. Physisorption and ortho–para conversion of molecular hydrogen on solid surfaces. *Progress in surface science*, 88(4):279–348, 2013.

[20] HP Gush, EJ Allin, HL Welsh, and WFJ Hare. The infrared fundamental band of liquid and solid hydrogen. *Canadian Journal of Physics*, 38(2):176–193, 1960.

[21] Ashok Bhandari, Alexandar P Rollings, Levi Ratto, and Jonathan D Weinstein. High-purity solid parahydrogen. *Review of Scientific Instruments*, 92(7):073202, 2021.

[22] Ashok Bhandari, Alexandar Rollings, and Jonathan Weinstein. High-purity solid parahydrogen for trapping atoms and molecules. *Bulletin of the American Physical Society*, 2021.

[23] Takeshi Oka. High-resolution spectroscopy of solid hydrogen. *Annual Review of Physical Chemistry*, 44(1):299–333, 1993.

[24] Simon Tam and Mario E Fajardo. Ortho/para hydrogen converter for rapid deposition matrix isolation spectroscopy. *Review of Scientific Instruments*, 70(4):1926–1932, 1999.

[25] Yu-Jong Wu, Xueming Yang, and Yuan-Pern Lee. Infrared matrix-isolation spectroscopy using pulsed deposition of p-h 2. *The Journal of chemical physics*, 120(3):1168–1171, 2004.

[26] Lester Andrews and Xuefeng Wang. Simple ortho-para hydrogen and para-ortho deuterium converter for matrix isolation spectroscopy. *Review of scientific instruments*, 75(9):3039–3044, 2004.

[27] Brian A Tom, Siddhartha Bhasker, Yuki Miyamoto, Takamasa Momose, and Benjamin J McCall. Producing and quantifying enriched para-h2. *Review of Scientific Instruments*, 80(1):016108–016108, 2009.

[28] K Sundararajan, K Sankaran, N Ramanathan, and R Gopi. Production and characterization of para-hydrogen gas for matrix isolation infrared spectroscopy. *Journal of Molecular Structure*, 1117:181–191, 2016.

[29] Masashi Tsuge and Yuan-Pern Lee. Spectroscopy of molecules confined in solid para-hydrogen. In *Molecular and Laser Spectroscopy*, pages 167–215. Elsevier, 2020.

[30] Andrew N Kanagin. *Creation and Analysis of Para-Hydrogen Crystals*. Bachelor's thesis, University of Nevada, Reno, 2015.

[31] Kyle Hardman. *Closed cycle liquid He Cryogenic Cooler: Towards Controlling Chemical Reactions*. Masters thesis, University of Nevada, Reno, 2011.

[32] Agilent Scientific Instruments. TwisTorr 84 FS. Model: X3502-69001, Serial number: IT17261045.

[33] Cryogenic Control Systems, Inc. S950 silicon diode sensor., Uncalibrated , https://www.cryocon.com/CCdownload/Sensors/S900/s950curve.pdf.

[34] Cryogenic Control Systems, Inc. DT-670 silicon diode sensor., Band B1, https://www.lakeshore.com/products/categories/specification/temperature-products/cryogenic-temperature-sensors/dt-670-silicon-diodes.

[35] MKS Instruments. 910 DualTrans Transducer. Part number: 910-12024, Serial number: 910A0303.

[36] Extorr Inc. Model XT300. Serial number: 3390.

[37] MKS Instruments. Mass flow controller. Part number: GE50A007201RBV020, Trace code: 022709352.

[38] Thorlabs Inc. CaF2 Plano-Convex Lens, f = 500 mm, Uncoated. Part number: LA5464.

[39] STMicroelectronics. LM317T. Part number: 497-1575-5-ND.

[40] Texas Instruments. LM234. Part number: LM234Z-6/NOPB-ND.

[41] National Instruments. PCIe-6321, X Series DAQ (16 AI, 24 DIO, 2 AO), HTS:8471804000, ECCN: EAR99, Part number: 781044-01.

[42] National Instruments. CB-68LPR I/O Connector Block, HTS: 8536904000, ECCN: 3A992.a, Part number: 777145-02.

[43] Cryomech Inc. PT415. `https://www.cryomech.com/products/pt415/`.

[44] AVX Corporation. 100 Ohms ±5% 20 W Thin Film Chassis Mount Resistor. Manufacturer Part Number: RP60300R0100JNBK, Digi-Key Part Number 478-7034-ND.

[45] Thorlabs Inc. AR coated wedged sapphire window. Part number: WW31050-D.

[46] Swagelok. Flexible Corrugated Stainless Steel Tubing. Part number: 321-4-X-12-B2.

[47] McMaster-Carr. mooth-Bore Seam-less Stainless Steel Tubing. Part number: 89785K911.

[48] McMaster-Carr. Stainless Steel straight reducer. Part number: 5182K242.

[49] National Instruments. LabVIEW. `https://http://www.ni.com/`.

[50] WaveMetrics Inc. IGOR Pro 8. `https://www.wavemetrics.com/`.

[51] Monika Hartl, Robert Chad Gillis, Luke Daemen, Daniel P Olds, Katherine Page, Stefan Carlson, Yongqiang Cheng, Thomas Hügle, Erik B Iverson, AJ Ramirez-Cuesta, et al. Hydrogen adsorption on two catalysts for the ortho-to parahydrogen conversion: Cr-doped silica and ferric oxide gel. *Physical Chemistry Chemical Physics*, 18(26):17281–17293, 2016.

[52] Mario E Fajardo. Solid parahydrogen thickness revisited. *Applied Spectroscopy*, 73(12):1403–1408, 2019.

[53] Anthony Crane and HP Gush. The induced infrared absorption spectrum of solid deuterium and solid hydrogen deuteride. *Canadian Journal of Physics*, 44(2):373–398, 1966.

[54] J Van Kranendonk and G Karl. Theory of the rotational and vibrational excitations in solid parahydrogen, and frequency analysis of the infrared and raman spectra. *Reviews of Modern Physics*, 40(3):531, 1968.

[55] Mario E Fajardo. Matrix isolation spectroscopy in solid parahydrogen: A primer. In Leonid Khriachtchev, editor, *Physics and Chemistry at Low Temperatures*, pages 167–202. Pan Stanford Publishing: Singapore, 2011.

[56] PL Raston, SC Kettwich, and DT Anderson. Infrared studies of ortho-para conversion at cl-atom and h-atom impurity centers in cryogenic solid hydrogen. *Low Temperature Physics*, 36(5):392–399, 2010.

[57] Mehran Kardar. Statistical physics of particles. Published in the United States of America by Cambridge University Press, New York, 2007. ISBN-10 0-521-87342-8, www.cambridge.org/9780521873420.

[58] PC Souers, CK Briggs, JW Pyper, and RT Tsugawa. Hydrogen vapor pressures from 4 to 30 k: a review.[67 references]. Technical report, California Univ., Livermore (USA). Lawrence Livermore Lab., 1977.

[59] E Matar, H Bergeron, F Dulieu, H Chaabouni, M Accolla, and JL Lemaire. Gas temperature dependent sticking of hydrogen on cold amorphous water ice surfaces of interstellar interest. *The Journal of chemical physics*, 133(10):104507, 2010.

[60] H Chaabouni, H Bergeron, S Baouche, F Dulieu, E Matar, E Congiu, L Gavilan, and JL Lemaire. Sticking coefficient of hydrogen and deuterium on silicates under interstellar conditions. *Astronomy & Astrophysics*, 538:A128, 2012.

[61] J. E. Sansonetti, W. C. Martin, and S. L. Young. *Handbook of Basic Atomic Spectroscopic Data*. National Institute of Standards and Technology, 2013. http://physics.nist.gov/Handbook.

[62] I. Alekseev, Ev. Arkhipov, S. Bondarenko, O. Fedorchenko, V. Ganzha, K. Ivshin, P. Kammel, P. Kravtsov, C. Petitjean, V. Trofimov, A. Vasilyev, T. Vasyanina, A. Vorobyov, and M. Vznuzdaev. Cryogenic distillation facility for isotopic purification of protium and deuterium. *Review of Scientific Instruments*, 86(12):125102, 2015.

[63] Zhou Junbo, Gao Liping, and Wang Kuisheng. Hydrogen isotope separation by cryogenic gas chromatography using the combined column of 5 å molecular sieve and al2o3. *International journal of hydrogen energy*, 31(14):2131–2135, 2006.

[64] Britney D Lorenz and David T Anderson. Infrared spectra of n 2 o–(ortho-d 2) n and n 2 o–(hd) n clusters trapped in bulk solid parahydrogen. *The Journal of chemical physics*, 126(18):184506, 2007.

[65] Simon Tam and Mario E. Fajardo. Ortho/para hydrogen converter for rapid deposition matrix isolation spectroscopy. *Review of Scientific Instruments*, 70(4):1926–1932, 1999.

[66] Kazuki Yoshioka , Paul L Raston, and David T Anderson. Infrared spectroscopy of chemically doped solid parahydrogen. *International Reviews in Physical Chemistry*, 25(3):469–496, 2006.

[67] Kazuki Yoshioka and David T Anderson. Infrared spectra of ch 3 f (ortho-h 2) n clusters in solid parahydrogen. *The Journal of chemical physics*, 119(9):4731–4742, 2003.